SUSY-QCD corrections to stop annihilation into electroweak final states including Coulomb enhancement effects

J. Harz, B. Herrmann, M. Klasen, K. Kovarik, M. Meinecke

▶ **To cite this version:**

HAL Id: hal-01116350

https://hal.archives-ouvertes.fr/hal-01116350

Submitted on 13 Feb 2015

SUSY-QCD corrections to stop annihilation into electroweak final states including Coulomb enhancement effects

J. Harz,[1, *] B. Herrmann,[2, †] M. Klasen,[3, ‡] K. Kovařík,[3, §] and M. Meinecke[3, ¶]

[1] *Department of Physics and Astronomy, University College London, London WC1E 6BT, United Kingdom*
[2] *LAPTh, Université de Savoie, CNRS, 9 Chemin de Bellevue, B.P. 110, F-74941 Annecy-le-Vieux, France*
[3] *Institut für Theoretische Physik, Westfälische Wilhelms-Universität Münster,*
Wilhelm-Klemm-Straße 9, D-48149 Münster, Germany
(Dated: November 18, 2014)

We present the full $\mathcal{O}(\alpha_s)$ supersymmetric QCD corrections for stop-anti-stop annihilation into electroweak final states within the Minimal Supersymmetric Standard Model (MSSM). We also incorporate Coulomb corrections due to gluon exchange between the incoming stops. Numerical results for the annihilation cross sections and the predicted neutralino relic density are presented. We show that the impact of the radiative corrections on the cosmologically preferred region of the parameter space can become larger than the current experimental uncertainty, shifting the relic bands within the considered regions of the parameter space by up to a few tens of GeV.

PACS numbers: 12.38.Bx,12.60.Jv,95.30.Cq,95.35.+d

I. INTRODUCTION

There exists convincing evidence today for a sizable Cold Dark Matter (CDM) component in the universe, stemming from a large variety of astronomical observations, such as rotation curves of galaxies, the Bullet Cluster, structure formation simulations on cosmological scales and the Cosmic Microwave Background (CMB). The most recent measurement of the CMB carried out by the Planck collaboration [1] in combination with WMAP data [2] has led to a precise determination of the dark matter relic density

$$\Omega_{\text{CDM}} h^2 = 0.1199 \pm 0.0027, \quad (1.1)$$

with h denoting the present Hubble expansion rate in units of 100 km s^{-1} Mpc^{-1}.

Since within the Standard Model (SM) there is no dark matter candidate which could solely account for the correct value of $\Omega_{\text{CDM}} h^2$, extensions of the SM which can provide an adequate DM candidate are necessary. Among the most prominent candidates are the so called WIMPs, Weakly Interacting Massive Particles. They naturally arise within certain theories beyond the standard model, e.g., the four neutralinos $\tilde{\chi}_i^0$ ($i = \{1, ..., 4\}$) within the MSSM. By further assuming R-parity conservation, the lightest neutralino $\tilde{\chi}_1^0$, which is for many realizations of the MSSM also the lightest supersymmetric particle (LSP), can become stable and is therefore a viable DM candidate.

In the following, we will sketch a general way of calculating the neutralino relic density $\Omega_{\tilde{\chi}_1^0} h^2$. We consider the case of N species of unstable particles χ_i which are heavier than the lightest particle denoted here by χ_0. We further assume that the time evolution of their number densities n_i is well described by a system of coupled Boltzmann equations [3],

$$\frac{dn_i}{dt} = -3Hn_i - \langle \sigma_{ij} v_{ij} \rangle \left[n_i n_j - \left(n_i^{\text{eq}} n_j^{\text{eq}} \right) \right], \quad (1.2)$$

for $i, j = 0, 1, \ldots, N$. The first term on the right-hand side of Eq. (1.2) containing the Hubble parameter H stands for the dilution of the particle number density due to the expansion of the universe, while the second and third terms describe the creation and (co)annihilation of the particle species χ_i and χ_j. $n_{i,j}^{\text{eq}}$ stands for the equilibrium number density of the particle species χ_i or χ_j, respectively, and $\langle \sigma_{ij} v_{ij} \rangle$ is the thermally averaged (co)annihilation cross section of χ_i and χ_j multiplied by their relative velocity v_{ij}.

As all particles will at some point decay into the lightest particle χ_0, the quantity relevant to estimate $\Omega_\chi h^2$ is the total number density $n_\chi = \sum_{i=0}^{N} n_i$. Using $n_i/n_\chi \approx n_i^{\text{eq}}/n_\chi^{\text{eq}}$ its time dependence can be expressed in the following form

$$\frac{dn_\chi}{dt} = -3Hn_\chi - \langle \sigma_{\text{ann}} v \rangle \left[n_\chi^2 - \left(n_\chi^{\text{eq}} \right)^2 \right]. \quad (1.3)$$

Here we have introduced the thermally averaged cross section [4]

$$\langle \sigma_{\text{ann}} v \rangle = \sum_{ij} \langle \sigma_{ij} v_{ij} \rangle \frac{n_i^{\text{eq}}}{n_\chi^{\text{eq}}} \frac{n_j^{\text{eq}}}{n_\chi^{\text{eq}}} \quad (1.4)$$

$$= \frac{\int_0^\infty dp_{\text{eff}} \, p_{\text{eff}}^2 W_{\text{eff}} K_1(\sqrt{s}/T)}{m_0^4 T \left[\sum_i \frac{g_i}{g_0} \frac{m_i^2}{m_0^2} K_2(m_i/T) \right]^2},$$

with K_i being the modified Bessel of second kind of order i and

$$W_{\text{eff}} = \sum_{ij} \frac{p_{ij}}{p_{\text{eff}}} \frac{g_i g_j}{g_0^2} W_{ij}. \quad (1.5)$$

* j.harz@ucl.ac.uk
† herrmann@lapth.cnrs.fr
‡ michael.klasen@uni-muenster.de
§ karol.kovarik@uni-muenster.de
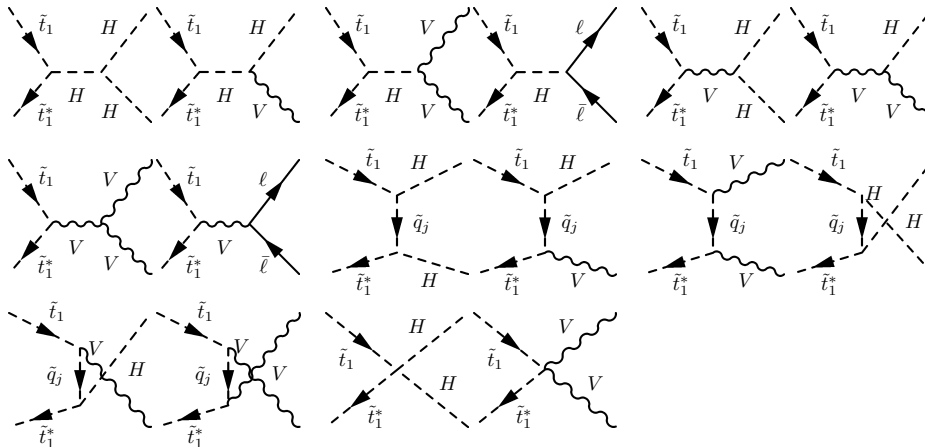¶ mmein_03@uni-muenster.de

FIG. 1. Tree-level diagrams contributing to the stop annihilation into electroweak SM final states. Here, $V = \gamma, Z^0, W^\pm$, $H = h^0, H^0, A^0, H^\pm$ and ℓ ($\bar{\ell}$) can be any (anti)lepton.

In Eq. (1.5), p_{ij} stands for the absolute value of the three-momentum of χ_i (or χ_j) in the center-of-mass frame of the (χ_i–χ_j) pair ($p_{\text{eff}} = p_{00}$) and

$$W_{ij} = \frac{1}{g_i g_j S_f} \sum_{\substack{\text{internal} \\ \text{d.o.f.}}} \int |\mathcal{M}|^2 (2\pi)^4$$

$$\delta^4(p_i + p_j - \sum_f p_f) \prod_f \frac{d^3 \mathbf{p}_f}{(2\pi)^3 2E_f} \qquad (1.6)$$

for a general n-body final state with momenta p_f. Finally, S_f is a symmetry factor, which accounts for identical particles in the final state and g_i (g_j) stands for the number of internal degrees of freedom of the particular species. As it will be important in the following analysis, we recall that the ratios $n_i^{\text{eq}}/n_\chi^{\text{eq}}$ in Eq. (1.4) at temperature T are Boltzmann suppressed via

$$\frac{n_i^{\text{eq}}}{n_\chi^{\text{eq}}} \sim \exp\left[-\frac{m_i - m_0}{T}\right]. \qquad (1.7)$$

Thus, only particles with a mass close to m_0 can give important contributions to $\langle \sigma_{\text{ann}} v \rangle$ and are able to sizably alter the time dependence of n_χ. After solving the Boltzmann equation, today's relic density is given by

$$\Omega_\chi = \frac{m_\chi n_\chi}{\rho_{\text{crit}}}, \qquad (1.8)$$

with n_χ and ρ_{crit} being today's particle number density and the critical density of the Universe, respectively.

For large parts of the MSSM parameter space an enhancement of the neutralino annihilation cross section is necessary to drive the relic density $\Omega_{\tilde{\chi}_1^0} h^2$ to the experimentally favored region of Eq. (1.1). One mechanism, which can yield such an enhancement, is the so-called coannihilation between the LSP and the next-to-lightest supersymmetric particle (NLSP), see Eq. (1.4) [5, 6].

Over wide ranges of the MSSM parameter space the lighter stop $\tilde{t}_1$ is the NLSP. If $m_{\tilde{\chi}_1^0} \approx m_{\tilde{t}_1}$, the coannihilations are no longer suppressed (see Eq. (1.7)) and so the coannihilations of the lightest neutralino with the light stop are the leading mechanism which determines the relic density of neutralino dark matter. This is not the whole story, though. If the mass difference between the stop and the lightest neutralino is even smaller, the dominating processes actually turn out to be the stop-anti-stop annihilation although they are normally doubly suppressed by the same factor as the coannihilations given by Eq. (1.7) [8].

Furthermore, it is well known that the (co)annihilation cross sections can become quite sensitive to higher order corrections. Therefore, the impact of next-to-leading order (NLO) corrections on the neutralino relic density has been explored in many previous analyses, e.g., SUSY-QCD corrections to neutralino-pair annihilation and coannihilation with heavier neutralinos and charginos into quarks [9–11] or SUSY-QCD corrections to neutralino-stop coannihilation [12–14]. Electroweak (EW) corrections to neutralino-pair annihilation and coannihilation with another gaugino have been investigated in Ref. [15]. Further studies rely on effective coupling approaches to capture certain classes of corrections to neutralino-pair annihilation or coannihilation with a tau slepton [16, 17]. All these analyses have shown the significance of higher order corrections to (co)annihilation channels for a precise prediction of $\Omega_{\tilde{\chi}_1^0} h^2$, which can even by far exceed the current experimental uncertainty given in Eq. (1.1)[1].

Motivated by these results, we have calculated the full $\mathcal{O}(\alpha_s)$ SUSY-QCD corrections to stop annihilation into

---

[1] See also [18] for a recent investigation on the applicability of the formalism presented here in the context of NLO calculations.

electroweak final states (i.e. leptons, vector and Higgs bosons)

$$\tilde{t}_1 \tilde{t}_1^* \rightarrow VV, \tag{1.9}$$

$$\tilde{t}_1 \tilde{t}_1^* \rightarrow VH, \tag{1.10}$$

$$\tilde{t}_1 \tilde{t}_1^* \rightarrow HH, \tag{1.11}$$

$$\tilde{t}_1 \tilde{t}_1^* \rightarrow \ell\bar{\ell}, \tag{1.12}$$

with $V = \gamma, Z^0, W^\pm$ and $H = h^0, H^0, A^0, H^\pm$. The corresponding Feynman diagrams at the tree level are shown in Fig. 1. We further have taken into account the corresponding Coulomb corrections due to the exchange of soft gluons between the initial stop-anti-stop pair. Their importance to $\Omega_{\tilde{\chi}_1^0} h^2$ has been discussed in Refs. [12, 19]. Our corrections to the given channels enter the total cross section σ_{ann} in the Boltzmann equation (1.3). They are included in our computer package called DM@NLO, which can be linked to public codes like micrOMEGAs [20] or DarkSUSY [21] to obtain the final corrected relic density. Up to now both of these codes evaluate the (co)annihilation cross sections just at an effective tree level such that the results of this work present a natural extension.

This paper is organized as follows: In Sec. II we specify the model framework, introduce our reference scenarios and discuss the phenomenology of stop annihilation into the electroweak final states mentioned in Eqs. (1.9)

– (1.12). Sec. III contains technical details about the actual cross section calculation. There, we discuss in particular our handling of ultraviolet (UV) and infrared (IR) divergences as well as the treatment of the Coulomb corrections. In Sec. IV we present our numerical results to illustrate the impact of our corrections on the cross section and the relic density. Finally, our conclusions are given in Sec. V.

II. PHENOMENOLOGY OF STOP ANNIHILATION

As discussed in Sec. I, we study the impact of higher-order SUSY-QCD corrections to stop annihilation on the neutralino relic density $\Omega_{\tilde{\chi}_1^0} h^2$. We have already mentioned above that in order for these processes to become phenomenologically relevant, we have to assume the lightest scalar top to be almost mass degenerate with the lightest neutralino. This assumption is motivated by the latest LHC data, where SUSY scenarios with a light third squark generation are able to reduce fine tuning while still evading the LHC exclusion limits [22, 23].

The existence of a light stop gets further support from the LHC discovery of a new boson with a mass of $m \approx 125$ GeV [24–26]. If we interpret it as the light "SM-like" Higgs boson h^0, its mass has to be enhanced, e.g., by a large stop loop contribution, which in the decoupling limit $m_{A^0} \gg m_{Z^0}$ takes the form [27, 28]

$$m_{h^0}^2 \approx m_{Z^0}^2 \cos^2 2\beta + \frac{3g^2 m_t^4}{8\pi^2 m_{W^\pm}^2} \left[\ln\left(\frac{M_{\text{SUSY}}^2}{m_t^2} \right) + \frac{X_t^2}{M_{\text{SUSY}}^2} \left(1 - \frac{X_t^2}{12 M_{\text{SUSY}}^2} \right) \right], \tag{2.1}$$

where $X_t = A_t - \mu \tan \beta$ and $M_{\text{SUSY}} = \sqrt{m_{\tilde{t}_1} m_{\tilde{t}_2}}$. For these contributions to become sufficiently large, $|X_t| \approx \sqrt{6} M_{\text{SUSY}}$ should be fulfilled, which hints towards a sizable A_t and therefore towards a large stop mass splitting $m_{\tilde{t}_1} \ll m_{\tilde{t}_2}$ driving $\tilde{t}_1$ to be rather light.

Throughout this analysis we will work within the phenomenological MSSM (pMSSM), where the soft breaking parameters are fixed at the input scale $Q = 1$ TeV according to the SPA convention [29]. Out of the nineteen parameters, which usually span the pMSSM parameter space, we restrict ourselves to the following set of eleven free parameters: The Higgs sector is fixed by the higgsino mass parameter μ, the ratio $\tan \beta$ of the vacuum expectation values of the two Higgs doublets, and the pole mass m_{A^0} of the pseudoscalar Higgs boson. For the first and second generation squarks we introduce a common soft breaking mass parameter $M_{\tilde{q}_{1,2}}$, while the mass parameters for the third generation squarks are given by $M_{\tilde{q}_3}$ for sbottoms and left-handed stops as well as $M_{\tilde{u}_3}$ for right-handed stops. We further set all trilinear couplings to zero except for A_t, the trilinear coupling of the stop

sector. In contrast to the three independent mass parameters in the squark sector, we only use a single parameter $M_{\tilde{\ell}}$ as a soft breaking mass for all sleptons. Finally, since we do not assume gaugino mass unification, the gaugino sector is defined by three independent parameters M_1, M_2 and M_3, the bino, wino and gluino masses, respectively.

Phenomenologically interesting scenarios have to fulfill a certain number of constraints. For our scenario search we have considered the following prominent observables:

$$0.1145 \leq \Omega_{\tilde{\chi}_1^0} h^2 \leq 0.1253, \tag{2.2}$$

$$120 \text{ GeV} \leq m_{h^0} \leq 130 \text{ GeV}, \tag{2.3}$$

$$2.56 \cdot 10^{-4} \leq \text{BR}(b \rightarrow s\gamma) \leq 4.54 \cdot 10^{-4}, \tag{2.4}$$

$$|\delta a_\mu| < 288 \cdot 10^{-11}. \tag{2.5}$$

They have been selected for the following reasons: In order to work with scenarios, which respect the recent Planck measurements, we require the neutralino relic density to lie within the limits given in Eq. (2.2) at 2σ confidence level. This means that we expect the neu-

TABLE I. Input parameters for three selected reference scenarios in the pMSSM. All values except $\tan\beta$ are given in GeV.

	$\tan\beta$	μ	m_{A^0}	M_1	M_2	M_3	$M_{\tilde{q}_{1,2}}$	$M_{\tilde{q}_3}$	$M_{\tilde{u}_3}$	$M_{\tilde{\ell}}$	A_t
Ia	16.3	2653.1	1917.9	750.0	1944.1	5832.4	3054.3	2143.7	1979.0	2248.3	-3684.1
Ib	16.3	2653.1	1917.9	989.0	1944.1	5832.4	3054.3	2143.7	2159.0	2248.3	-3684.1
II	27.0	2650.8	1441.5	1300.0	1798.4	1744.8	2189.7	2095.3	1388.0	1815.5	-4097.9

TABLE II. Physical squark, neutralino, chargino and Higgs masses, the bino ($\tilde{B}$) contribution to $\tilde{\chi}_1^0$, the decomposition of $\tilde{t}_1$ into left- and right-handed parts, and selected observables corresponding to the reference scenarios of Tab. I. All masses are given in GeV.

	$m_{\tilde{\chi}_1^0}$	$m_{\tilde{t}_1}$	$m_{\tilde{t}_2}$	$m_{\tilde{b}_1}$	$m_{\tilde{\chi}_2^0}$	$m_{\tilde{\chi}_1^\pm}$	m_{h^0}	m_{H^0}	$m_{H^\pm}$	$|Z_{\tilde{\chi}^0,1\tilde{B}}|^2$	$|Z_{\tilde{t},1L}|^2$	$|Z_{\tilde{t},1R}|^2$	BR($b \to s\gamma$)	δa_μ	$\Omega_{\tilde{\chi}_1^0}h^2$
Ia	758.0	826.1	1435.1	1260.5	1986.7	1986.8	128.8	1917.4	1919.6	0.9996	0.27	0.74	$3.1 \cdot 10^{-4}$	$284 \cdot 10^{-11}$	0.1146
Ib	999.6	1079.6	1543.4	1265.8	1986.8	1986.9	129.4	1917.9	1919.6	0.9995	0.55	0.46	$3.1 \cdot 10^{-4}$	$284 \cdot 10^{-11}$	0.1193
II	1306.3	1363.0	2128.8	2055.2	1826.9	1827.1	124.6	1440.7	1443.6	0.9992	0.08	0.92	$3.1 \cdot 10^{-4}$	$279 \cdot 10^{-11}$	0.1209

TABLE III. Most relevant stop annihilation channels into EW final states of the reference scenarios in Tab. I.

	Scenario Ia	Scenario Ib	Scenario II
$\tilde{t}_1\tilde{t}_1^* \to h^0h^0$	46.1%	15.9%	11.3%
h^0H^0	–	46.6%	11.1%
$\tilde{t}_1\tilde{t}_1^* \to Z^0A^0$	–	4.0%	7.4%
$W^\pm H^\mp$	–	4.2%	13.6%
$\tilde{t}_1\tilde{t}_1^* \to Z^0Z^0$	8.7%	4.3%	7.4%
W^+W^-	12.5%	2.7%	13.6%
Total	67.3%	77.7%	64.4%

tralino to account for the whole amount of dark matter in our Universe today. Second, we require the mass of the lightest Higgs boson to agree with the observation at the LHC. However, we allow for a rather large uncertainty of about 5 GeV on the Higgs mass value due to large theoretical uncertainties arising from not yet included higher order corrections in its calculation (see e.g. Ref. [30]). The third bound, Eq. (2.4), concerns the inclusive branching ratio of the flavor changing neutral current decay $b \to s\gamma$. The imposed interval corresponds to the latest HFAG value [31] at 3σ confidence level. The fourth bound limits the supersymmetric corrections δa_μ to the muon g-factor g_μ, where $a_\mu = (g_\mu - 2)/2$ and $\delta a_\mu = a_\mu^{\rm exp} - a_\mu^{\rm theo}$ is the discrepancy between experiment and the predicted theoretical value. We expect the SUSY corrections to improve on this discrepancy compared to the SM-prediction (see Ref. [32]).

To illustrate the numerical impact of our derived corrections, we introduce the three reference scenarios given in Tab. I, which have been found by performing a random scan of one million points within the previously defined pMSSM. Their parameter values are summarized in Tab. I. The corresponding particle masses, mixings and further observables are summarized in Tab. II.

Throughout our analysis we have used `SPheno 3.2.3` [33] to obtain the physical mass spectrum and related mixings from the given input parameters. The neutralino relic density, the contributions of individual (co)annihilation channels, and the numerical values of further observables such as the branching fraction $b \to s\gamma$ have been obtained by using `micrOMEGAs 2.4.1` with the standard `CalcHEP` [34] implementation of the MSSM. We only have introduced slight changes to stabilize the numerical evaluation of the occurring phase-space integrals (see Sec. III C). We have checked within our typical scenarios that these changes do not have a relevant impact on the predicted relic density. As can be seen in Tab. II the three selected scenarios fulfill the demanded constraints given in Eqs. (2.2) – (2.5).

In order to better understand the origin of the radiative corrections in our scenarios, we dissect all scenarios and show which processes are important in which parameter point. Moreover, we look into each process so that we can identify the dominating contributions. We start by listing the stop annihilation processes that we correct and which contribute more than 1% to $\langle \sigma_{\rm ann} v \rangle$ in Tab. III. Then, for each process in Tab. III, we list the underlying structure of sub-channel contributions in Tab. IV, i.e. the contributions of different diagram classes as shown in Fig. 1. We have grouped the contributions from quartic couplings (contribution denoted as Q), s-channel scalar exchange (denoted s_S), and the squark exchange in the t- and u-channels (t/u). The vector contributions s_V to the s-channel do not appear in Tab. IV as they turn out to be negligible within our reference scenarios (see below). The contributions from the corresponding squared matrix elements are denoted by $Q \times Q$, $s_S \times s_S$ and $t/u \times t/u$, while the interference terms are denoted by $Q \times s_S$, $Q \times t/u$ and $s_S \times t/u$. Note that negative values refer to destructive interferences. The percentages in Tab. IV are obtained for the center-of-mass momentum of the incoming particles $p_{\rm cm} = 200$ GeV, which is roughly the region where the thermal distribution in the integrand of Eq. (1.4) peaks for the scenarios presented here. Since we work in Feynman gauge, we add the contributions of the Goldstone bosons and the Faddeev-Popov ghosts to the particular vector boson final states.

Note that, as the incoming scalar-antiscalar configuration is CP-even and as all the relevant interactions are CP-conserving, every intermediate and final state has to be CP-even, too. This limits all possible final states such that pseudoscalar Higgs bosons can appear only in pairs or together with a suitable vector boson and are otherwise partial-wave suppressed (see Tab. III). Moreover, the same argument prohibits any exchange of pseudoscalars in the s-channel. Finally any s-wave annihilation through the s-channel exchange of vector bosons is forbidden due to conservation of total angular momentum (see Tab. IV).

In scenario Ia, we correct processes which contribute 67.3% to $\Omega_{\tilde{\chi}_1^0} h^2$. The scenario is characterized by a dominant contribution of the $h^0 h^0$ final state (46.1%), while final states which include one or more of the heavier Higgs bosons H^0, A^0, $H^\pm$ are too heavy to be kinematically accessible. One further encounters a relative dominance of the Higgs-Higgs final state over the vector-vector final states, where the latter contribute roughly 21% to the relic density. This can be traced back to an enhancement of the Higgs coupling to scalar top quarks as compared to all other relevant couplings, e.g., the gauge interactions of EW vector bosons to squarks. It is caused by the large top mass and the large trilinear coupling A_t needed to achieve a sizable stop-loop contribution to m_{h^0}. It is especially important in the case of t- and u-channels where the enhanced stop-Higgs/Goldstone-boson coupling enters twice. This results in large contributions and explains the overall dominance of the t/u subchannels as can be seen in Tab. IV. But although the massive vector final states get contributions from Goldstone bosons, which give rise to couplings as large as the usual Higgs couplings, their corresponding t/u-channels contributions are further suppressed by large propagators. This is due the fact that G^0 as a pseudoscalar only couples light and heavy squark mass eigenstates. Furthermore, the charged Goldstone boson $G^\pm$ connects up- and down-type squarks, which leads in scenario Ia to contributions of t- and u-channel diagrams where the exchanged particle is much heavier than the lighter stop $\tilde{t}_1$ and therefore to an overall propagator suppression of the Goldstone boson contributions to vector-vector final states relative to, e.g., the $h^0 h^0$ final state.

In scenario Ib, we correct diagrams which contribute 77.7% to $\Omega_{\tilde{\chi}_1^0} h^2$. The situation is quite similar to scenario Ia except for the lightest stop being heavy enough so that also heavier Higgs bosons are kinematically accessible. As the final state has to be CP-even, the only additional sizable contributions stem from the $h^0 H^0$, $Z^0 A^0$ as well as from the $W^\pm H^\mp$ final state (see Tab. III). Comparing the scenarios Ia and Ib, one can see a shift of the main contribution to the relic density away from the $h^0 h^0$ final state over to the $h^0 H^0$ final state, which is with 46.6% the most important channel of scenario Ib. This shift is mainly driven by the dominant t/u-channel contributions in Tab. IV. The special feature of the $h^0 H^0$ final state is that it is just kinematically allowed ($m_{h^0} + m_{H^0} \approx 2m_{\tilde{t}_1}$),

so that the final-state Higgs bosons do not have large momenta. Furthermore, the dominant contribution to any cross section contribution to $\Omega_{\tilde{\chi}_1^0} h^2$ comes from the region $\sqrt{s} \approx 2m_{\tilde{t}_1}$, which further limits the momenta of the incoming and also outgoing particles. For the $h^0 H^0$ final states the t- and u-channel propagators are therefore close to their mass shells whereas for the $h^0 h^0$ final state these propagators are still far off their mass shells, which translates into the $h^0 H^0$ final state being the leading contribution.

In scenario II, 64.4% of all contributions to $\Omega_{\tilde{\chi}_1^0} h^2$ are affected by our corrections. The mass difference between the squarks and the heavier Higgs boson leads to the same structure of relevant processes as in scenario Ib but in contrast to the two previously encountered scenarios, scenario II is chosen such that it gets roughly equal contributions from all possible vector and Higgs boson combinations in the final state.

It can further be seen in Tab. III that for all three scenarios there are no sizable contributions to $\Omega_{\tilde{\chi}_1^0} h^2$ from lepton-antilepton final states. However, our scans over the pMSSM parameter space will later show that leptonic final states are indeed important when their contribution is enhanced by a resonant Higgs exchange. This happens if $2m_{\tilde{t}_1} \approx m_{H^0}$.

The absence of final states in Tab. III containing one or more photons is due to the fact that the photon as the massless gauge boson of the abelian $U(1)$ does not possess any s-channel contributions. Furthermore, there are no Goldstone boson contributions to photons in the final state, which turned out to be the dominant contributions to the $Z^0 Z^0$ and $W^+ W^-$ final states as explained above. Finally, as the photon coupling to sfermions is diagonal in the squark mass eigenbasis, the $\tilde{t}_1$-annihilation lacks all contributions of photon-Higgs final states, which all together leads to the absence of final states containing one or two photons as encountered in Tab. III. All other (co)annihilation channels as, e.g., coannihilation with heavier neutralinos, charginos, sbottoms, etc. are irrelevant in our scenarios Ia/b and II as the mass gaps between all these particles and the lightest neutralino is already too large (see Tab. II). This prevents these particles from significantly changing $\Omega_{\tilde{\chi}_1^0} h^2$ due the Boltzmann suppression of Eq. (1.7).

III. TECHNICAL DETAILS

### A. Calculation of $\mathcal{O}(\alpha_s)$ corrections

The NLO cross section

$$\sigma_{\mathrm{NLO}} = \int_2 \mathrm{d}\sigma^{\mathrm{V}} + \int_3 \mathrm{d}\sigma^{\mathrm{R}} \qquad (3.1)$$

consists of the virtual ($\mathrm{d}\sigma^{\mathrm{V}}$) and the real emission contributions ($\mathrm{d}\sigma^{\mathrm{R}}$), which are integrated over the two- and three-particle phase space, respectively. Figs. 2 and 3

TABLE IV. Sub-processes for the channels of Tab. III contributing individually at least 0.1% at $p_{\rm cm} = 200$ GeV.

	$Q \times Q$	$Q \times s_S$	$Q \times t/u$	$s_S \times s_S$	$s_S \times t/u$	$t/u \times t/u$
Scenario Ia						
$\tilde{t}_1\tilde{t}_1^* \to \quad h^0h^0$	0.7%	-0.2%	-17.5%	–	2.4%	114.6%
Z^0Z^0	2.7%	-0.3%	-37.7%	-4.8%	4.2%	135.9%
W^+W^-	2.2%	-0.4%	-32.7%	-6.1%	6.1%	131.0%
Scenario Ib						
$\tilde{t}_1\tilde{t}_1^* \to \quad h^0h^0$	2.1%	-0.2%	-32.9%	–	1.5%	129.6%
h^0H^0	–	–	0.6%	–	-0.6%	100.0%
Z^0A^0	–	–	2.3%	-21.7%	10.3%	109.0%
$W^\pm H^\mp$	–	–	1.8%	-35.4%	32.9%	100.8%
Z^0Z^0	5.1%	-0.3%	-54.5%	-5.3%	4.3%	150.7%
W^+W^-	6.6%	-1.2%	-52.4%	-19.2%	18.7%	147.7%
Scenario II						
$\tilde{t}_1\tilde{t}_1^* \to \quad h^0h^0$	8.0%	-0.4%	-72.2%	–	1.8%	162.7%
h^0H^0	–	–	2.4%	–	-0.6%	98.2%
Z^0A^0	–	–	3.0%	-2.1%	1.4%	97.7%
$W^\pm H^\mp$	–	–	2.9%	-1.8%	0.8%	98.1%
Z^0Z^0	11.9%	-0.3%	-92.6%	-3.5%	3.1%	181.4%
W^+W^-	11.4%	-0.3%	-90.1%	-3.1%	3.0%	179.2%
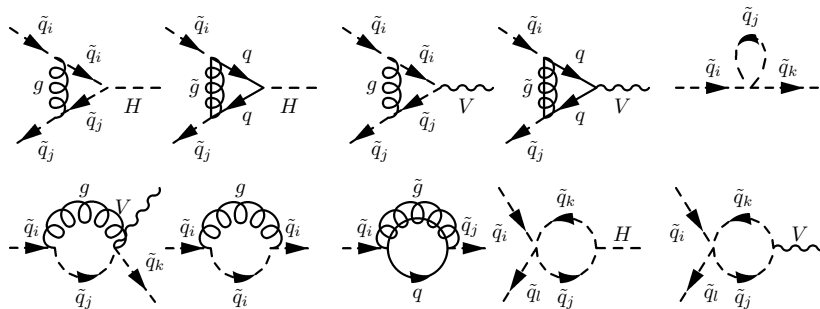
FIG. 2. Vertex and propagator insertions depicting schematically the one-loop corrections of $\mathcal{O}(\alpha_s)$ to the stop-annihilation processes shown in Fig. 1. Here, $V = \gamma, Z^0, W^\pm$ and $H = h^0, H^0, A^0, H^\pm$.

show the relevant one-loop diagrams for stop annihilation contributing to the virtual part $d\sigma^{\rm V}$. In Fig. 4 the corresponding real gluon emission diagrams corresponding to $d\sigma^{\rm R}$ are depicted.

The virtual SUSY-QCD corrections to stop annihilation include contributions from the exchange of gluons and gluinos as well as from pure squark loops. These corrections, calculated using the SUSY-preserving dimensional reduction ($\overline{\rm DR}$) scheme, can be all reduced via the Passarino-Veltman reduction to the well known scalar integrals A_0, B_0, C_0, and D_0 [35]. The ultraviolet (UV) divergences, which appear in the resulting expressions, can then be cancelled by properly chosen counterterms.

In our calculation, the latter are defined in a hybrid on-shell / $\overline{\rm DR}$ renormalization scheme, where A_t, A_b, $m_{\tilde{t}_1}^2$, $m_{\tilde{b}_1}^2$, and $m_{\tilde{b}_2}^2$ are chosen as input parameters along with

the heavy quark masses m_b and m_t. The strong coupling α_s, the trilinear couplings A_t, A_b and the bottom quark mass m_b are defined in the $\overline{\rm DR}$ scheme at the scale $\mu_R = 1$ TeV, which corresponds to the scale where the soft breaking parameters are defined. All remaining input masses are defined on-shell. A more detailed discussion of this particular renormalization scheme as well as of our treatment of α_s can be found in Refs. [13, 14].

Apart from the UV divergences, one-loop matrix elements also contain infrared (IR) divergences which arise due to the exchange of soft gluons in the loop. These IR divergences are also dimensionally regularized using the $\overline{\rm DR}$-scheme. The associated poles cancel against IR poles of the same form, but opposite sign stemming from the real corrections shown in Fig. 4 [36]. Since a completely analytic integration of Eq. (3.1) is in practice impossible for all but the simplest integrands, one usually
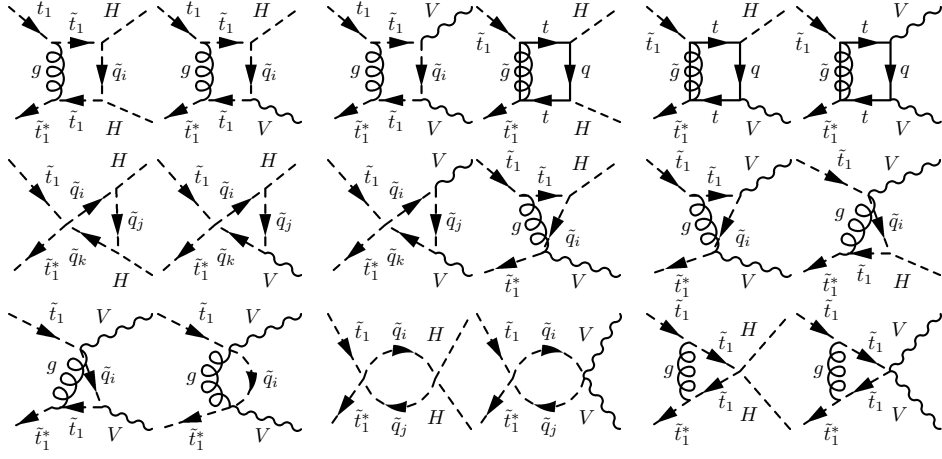
FIG. 3. Diagrams depicting corrections of $\mathcal{O}(\alpha_s)$ to the stop-annihilation processes shown in Fig. 1. As before, $V = \gamma, Z^0, W^\pm$ and $H = h^0, H^0, A^0, H^\pm$. The diagrams in the first row are in the following referred to as box contributions, whereas we subsume the diagrams of the second and third row under vertex corrections. u-channel processes are not explicitly shown, as they can be obtained by crossing from the corresponding t-channel diagrams.
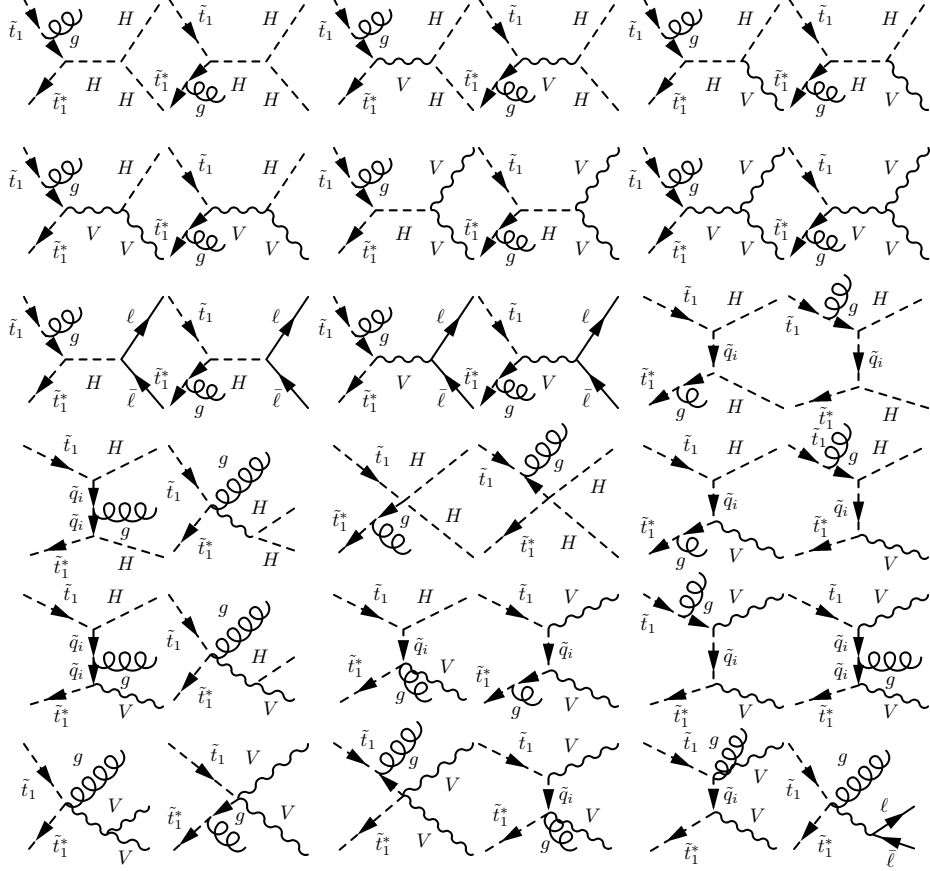

FIG. 4. Diagrams depicting the real gluon emission corrections of $\mathcal{O}(\alpha_s)$ to the stop-annihilation processes shown in Fig. 1. As before, $V = \gamma, Z^0, W^\pm$ and $H = h^0, H^0, A^0, H^\pm$. The corrections to the u-channel processes are not explicitly shown, as they can be obtained by crossing from the corresponding t-channel diagrams.

makes use of numerical integration. However, to render Eq. (3.1) numerically integrable, a matching of the IR singularities residing in the differential cross sections $d\sigma^{\rm V}$ and $d\sigma^{\rm R}$ is necessary. As these differential cross sections have to be integrated separately over different phase spaces, one cannot take advantage of the direct cancellation of the IR divergences between the real and virtual part. Especially, as the singularities of the real corrections actually arise during the integration over the $2 \to 3$ phase space, whereas the IR singularities of the virtual corrections can already be separated as poles before performing any $2 \to 2$ phase-space integration, this matching is far from being trivial. Multiple possibilities exist to integrate Eq. (3.1). One is the dipole subtraction method [37], a second one is the so-called phase space slicing method [35]. In this work we made use of the latter.

The phase-space slicing method isolates the IR divergence in the real corrections by slicing the $2 \to 3$ phase-space into two parts using a cut ΔE on the energy $|\vec{k}|$ of the additional gluon. In the soft-gluon region, where $|\vec{k}| \leq \Delta E$, we can approximate the $2 \to 3$ amplitudes and factorize them according to

$$\left(\frac{d\sigma}{d\Omega}\right)_{\rm soft} = F \times \left(\frac{d\sigma}{d\Omega}\right)_{\rm tree-level}, \quad (3.2)$$

where F already contains the integration over the gluon phase space with $|\vec{k}| \leq \Delta E$ and therefore all IR divergences. Furthermore, the integration in F can be performed analytically in $D = 4 - 2\epsilon$ dimensions such that a cancellation of the arising singularities against the IR singularities of the virtual corrections is already possible at the integrand level. The remaining part of the $2 \to 3$ phase space integration in Eq. (3.1), where $|\vec{k}| > \Delta E$, can then be performed numerically in $D = 4$ dimensions. Note that no collinear divergences occur in our case, since the additional gluon can be radiated only off a massive scalar.

The final sum of the soft-gluon approximation and the remaining $2 \to 3$ part should be independent of the unphysical cutoff ΔE on the gluon energy. In practice one has to choose a convenient value for ΔE. On the one hand, it should not be too small, because the phase space integration of the real corrections would be numerically unstable. On the other hand, the cut should also not be too large, not to invalidate the soft-gluon approximation of the cross section for $|\vec{k}| \leq \Delta E$. We verified that the full $2 \to 3$ cross sections are insensitive to a variation of ΔE around our choice of this cut. In addition, there are logarithms of the dimensional regularization scale μ, which we set equal to the renormalization scale $\mu = \mu_R = 1$ TeV. These logarithms, which arise in the soft-gluon approximation of the $2 \to 3$ processes as well as in the corresponding virtual contributions can give rise to an enhancement of both contributions separately, but cancel in the final sum of Eq. (3.1).
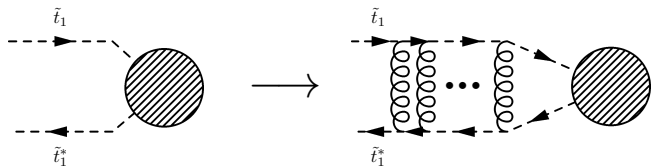

FIG. 5. Ladder diagram for a LO Coulomb potential.

B. Coulomb corrections

In the previous subsection, we have discussed the fixed-order corrections due to the exchange of one gluon, squark or gluino for the stop-antistop annihilation into electroweak final states. There are, however, additional potentially important corrections stemming from the exchange of multiple gluons between the stops in the initial state, which will be discussed in the following.
During the calculation of the $\mathcal{O}(\alpha_s)$ corrections of the previous subsection we encounter terms which are proportional to $1/v$, where v is the relative velocity of the incoming stop-antistop pair. It is well known that the exchange of n gluons generates a correction factor proportional to $(\alpha_s/v)^{\rm n}$, within the perturbative expansion in α_s.[2]

Since during freeze-out the stops are moving slowly $(E_{{\rm kin},\tilde{t}_1} \approx T_{\rm freeze-out} \ll m_{\tilde{t}_1})$, this fraction can become large,

$$\alpha_s/v \gtrsim \mathcal{O}(1), \quad (3.3)$$

and spoil the convergence of the perturbative series [38, 39]. Hence these so-called Coulomb corrections need to be resummed to all orders to get a reliable result (see Fig. 5). This can be done in the framework of non-relativistic QCD (NRQCD) [40]. Following Ref. [41], the Coulomb-corrected result can be cast into the form

$$\sigma^{\rm Coul.}\left(\tilde{t}_1\tilde{t}_1^* \to {\rm EW}\right) = \frac{4\pi}{vm_{\tilde{t}_1}^2}\Im\left\{G^{[1]}\left(\mathbf{r} = 0; \sqrt{s} + i\Gamma_{\tilde{t}_1}\right)\right\}$$
$$\times \sigma^{\rm LO}\left(\tilde{t}_1\tilde{t}_1^* \to {\rm EW}\right), \quad (3.4)$$

where $\sigma^{\rm LO}(\tilde{t}_1\tilde{t}_1^* \to {\rm EW})$ is the annihilation cross section of the stop-antistop color singlet into EW final states. $G^{[1]}\left(\mathbf{r}; \sqrt{s} + i\Gamma_{\tilde{t}_1}\right) = G^{[1]}\left(\mathbf{r}, \mathbf{r}' = 0; \sqrt{s} + i\Gamma_{\tilde{t}_1}\right)$ stands for the color-singlet Green's function of the Schrödinger equation at $\mathbf{r}' = 0$. It governs the dynamics of the would-be stoponium evaluated at distance $\mathbf{r}$. More precisely, $G^{[1]}\left(\mathbf{r}; \sqrt{s} + i\Gamma_{\tilde{t}_1}\right)$ is the solution to

$$\left[H^{[1]} - \left(\sqrt{s} + i\Gamma_{\tilde{t}_1}\right)\right]G^{[1]}\left(\mathbf{r}; \sqrt{s} + i\Gamma_{\tilde{t}_1}\right) = \delta^{(3)}(\mathbf{r}), \quad (3.5)$$

---

[2] The divergence at $v \to 0$ is the well-known Coulomb singularity signaling the production of a stop-antistop quasi-bound state, called stoponium.

with $H^{[1]}$ being the Hamilton operator of the stop-antistop system,

$$H^{[1]} = -\frac{1}{m_{\tilde{t}_1}}\Delta + 2m_{\tilde{t}_1} + V^{[1]}(\mathbf{r}). \tag{3.6}$$

The Fourier transform of the color-singlet Coulomb potential $V^{[1]}(\mathbf{r})$ can be written at NLO as [42, 43]

$$\tilde{V}^{[1]}(\mathbf{q}) = -\frac{4\pi\alpha_s(\mu_G)C^{[1]}}{\mathbf{q}^2} \tag{3.7}$$
$$\times \left[1 + \frac{\alpha_s(\mu_G)}{4\pi}\left(\beta_0 \ln\frac{\mu_G^2}{\mathbf{q}^2} + a_1\right)\right]$$

with

$$C^{[1]} = C_{\mathrm{F}} = \frac{4}{3}, \quad C_{\mathrm{A}} = 3,$$
$$a_1 = \frac{31}{9}C_A - \frac{20}{9}T_f n_f,$$
$$\beta_0 = \frac{11}{3}C_A - \frac{4}{3}T_f n_f, \tag{3.8}$$

and $T_f = \frac{1}{2}$ for top squarks. The zero-distance NLO Green's function is known in a compact analytic form,

$$G^{[1]}(0;\sqrt{s}+i\Gamma_{\tilde{t}_1}) = \frac{C^{[1]}\alpha_s(\mu_G)m_{\tilde{t}_1}^2}{4\pi} \tag{3.9}$$
$$\times\left[g_{\mathrm{LO}} + \frac{\alpha_s(\mu_G)}{4\pi}g_{\mathrm{NLO}} + \dots\right],$$

where its UV-divergence at $\mathbf{r} = 0$ has been removed via $\overline{\mathrm{MS}}$-subtraction [44]. We work with $n_f = 6$ active quark flavors and with α_s renormalized in the $\overline{\mathrm{MS}}$-scheme. In Eq. (3.9) we made use of the definitions

$$g_{\mathrm{LO}} = -\frac{1}{2\kappa} + L - \psi^{(0)},$$
$$g_{\mathrm{NLO}} = \beta_0\left[L^2 - 2L(\psi^{(0)} - \kappa\psi^{(1)}) + \kappa\psi^{(2)} + (\psi^{(0)})^2 - 3\psi^{(1)} - 2\kappa\psi^{(0)}\psi^{(1)} + 4\ _4F_3(1,1,1,1;2,2,1-\kappa;1)\right]$$
$$+a_1\left[L - \psi^{(0)} + \kappa\psi^{(1)}\right], \tag{3.10}$$

and

$$\kappa = \frac{iC^{[1]}\alpha_s(\mu_G)}{2v},$$
$$v = \sqrt{\frac{\sqrt{s}+i\Gamma_{\tilde{t}_1}-2m_{\tilde{t}_1}}{m_{\tilde{t}_1}}},$$
$$L = \ln\frac{i\mu_G}{2m_{\tilde{t}_1}v}. \tag{3.11}$$

Here, $\psi^{(n)} = \psi^{(n)}(1-\kappa)$ is the n-th derivative of $\psi(z) = \gamma_{\mathrm{E}} + \mathrm{d}/\mathrm{d}z \ln\Gamma(z)$ and $_4F_3(1,1,1,1;2,2,1-\kappa;1)]$ is a hypergeometric function (for further details see App. A). For the NLO Green's function in Eq. (3.4) μ_G can be chosen independently of the renormalization scale μ_R. Since the Coulomb corrections are related to the exchange of potential gluons with momentum $|\mathbf{p}| \approx m_{\tilde{t}_1}v$, taking μ_G of the order

$$\mu_G \sim m_{\tilde{t}_1}v \sim m_{\tilde{t}_1}\alpha_s \tag{3.12}$$

is expected to be a natural choice (see Eq. (3.3)). Hence we define μ_G to be [45]

$$\mu_G = \max\{C^{[1]}m_{\tilde{t}_1}\alpha_s(\mu_G), 2m_{\tilde{t}_1}v\}, \tag{3.13}$$

where $\mu_G = C^{[1]}m_{\tilde{t}_1}\alpha_s(\mu_G)$ corresponds to twice the inverse Bohr radius. It has been shown in Ref. [46] for the

color singlet top-anti-top pair production near threshold, that with μ_G set to this characteristic (s)quarkonium-energy scale, the Green's function possesses a well convergent perturbative series.

To avoid double counting of NLO corrections, which are included in the Green's function as well as in our full NLO calculation (see, e.g., the first diagram of Fig. 3), we have to subtract the one-loop contribution

$$\Im\left\{G^{[1]}(0;\sqrt{s}+i\Gamma_{\tilde{t}_1})\right\} = \tag{3.14}$$
$$m_{\tilde{t}_1}^2\Im\left\{\frac{v}{4\pi}\left[i + \frac{\alpha_s(\mu_G)C^{[1]}}{v}\left(\frac{i\pi}{2} + \ln\frac{\mu_G}{2m_{\tilde{t}_1}v}\right) + \mathcal{O}(\alpha_s^2)\right]\right\}$$

from Eq. (3.9). Eq. (3.14) has been obtained by expanding Eq. (3.9) up to $\mathcal{O}(\alpha_s^2)$.

Setting μ_G in Eq. (3.14) to the hard scale $\mu_G = 1$ TeV and renormalizing α_s according to Sec. III A, we find a matching between the Coulomb enhanced diagrams of the full NLO calculation and the Coulomb corrections expanded up to $\mathcal{O}(\alpha_s^2)$ in the threshold region with a precision better than 1%.

Another subtlety arises as Eq. (3.10) is only an expansion around the leading-order bound-state poles. It therefore induces poles in the Green's function of the general form $\left[\alpha_s E_n^{\mathrm{LO}}/(E_n^{\mathrm{LO}} - \sqrt{s} - i\Gamma_{\tilde{t}_1})\right]^k$ (k=1,2 at NLO), which differ by an $\mathcal{O}(\alpha_s^2)$ correction from an exact treatment [42, 47]. Hence this difference only becomes rele-

vant in the vicinity of the associated bound-state poles. But as their production is suppressed by the non-zero temperature during freeze-out[3], there is no need for a more elaborated treatment in terms of a precise calculation of $\Omega_{\tilde{\chi}_1^0} h^2$.

Finally note, that the approach presented here implicitly assumes that the amplitudes, which enter σ^{LO} in Eq. (3.4), do not depend on the momenta of the annihilating particles. In the case of dominant s-wave annihilation in the non relativistic limit this is a well justified approximation but turns out to be misleading for cross sections dominated by, e.g., the p-wave contribution. For these cases the Coulomb corrections for a leading order Coulomb potential can be found in Refs. [48, 49]. Since we provide a complete NLO calculation, the error turns out to be of the order $\mathcal{O}(\alpha_s^2)$ for $\alpha_s \ll v$ and remains of this order relative to the leading $\mathcal{O}((\alpha_s/v)^n)$ Coulomb corrections even in the limit $\alpha_s \gtrsim v$. Hence we chose to rely on this simplified treatment.

In Fig. 6, we compare cross sections which include the Coulomb corrections to the corresponding tree-level cross sections for two processes of scenario II. We chose scenario II for presenting our results, but it should be noted that the basic qualitative behavior is scenario-independent. The grey shaded areas represent the thermal averaging function in Eq. (1.4) in arbitrary units and indicate the thermal weighting of the σv contribution to $\Omega_{\tilde{\chi}_1^0} h^2$.

We show the stop-annihilation into the $h^0 H^0$ and $W^+ W^-$ final state. In both cases a steep rise of the Coulomb-corrected σv (green line) is observed for low p_{cm} due to the attractive force felt by the stop-anti-stop pair (see Eq. (3.7)), whereas the tree level (orange line), which is dominated by s-wave annihilation of the $\tilde{t}_1 \tilde{t}_1^*$ pair, is roughly constant. For higher p_{cm} values, the $1/v$-enhancement becomes more and more subdominant, and the Coulomb corrections turn into a usual perturbative series in α_s. Although the Coulomb corrections become very large only in the region where the thermal distribution is small, Fig. 6 can still elucidate the relevance of these corrections for a precision calculation of $\Omega_{\tilde{\chi}_1^0} h^2$.

C.   Further subtleties

Some of the $2 \to 2$ amplitudes, which contribute to the final neutralino relic density $\Omega_{\tilde{\chi}_1^0} h^2$, contain a gluon and an unstable electroweak particle X, such as a Higgs or a Z-boson, in their final state. By further adding the $2 \to 3$ processes as, e.g., the diagrams of the first line of Fig. 4 we partly double-count some of these contributions. The

reason is that in the case of an on-shell Higgs or vector boson propagator, the $2 \to 3$ amplitude corresponds to the on-shell production of a gluon and a heavy boson X followed by its decay, which is already included within the $2 \to 2$ processes (exemplified in Fig. 7).

To avoid this double counting, we subtract from the usual $2 \to 2$ matrix element the $2 \to 2$ matrix element weighted by the fraction of the EW decay width $\Gamma_{X \to \text{EW}}$ divided by the total decay width $\Gamma_{X \to \text{tot}}$, both for a two particle final state. More precisely, we have introduced the replacement

$$\left| M_{\tilde{t}_1 \tilde{t}_1^* \to Xg} \right|^2 \to \left(1 - \frac{\Gamma_{X \to \text{EW}}}{\Gamma_{X \to \text{tot}}} \right) \times \left| M_{\tilde{t}_1 \tilde{t}_1^* \to Xg} \right|^2. \quad (3.15)$$

Within our implementation it is in principal possible that in some rare cases a gluon-X final state is corrected as in Eq. (3.15) without that the corresponding $2 \to 3$ amplitude has been taken into account. But as we correct all processes, which contribute more than 1% to $\Omega_{\tilde{\chi}_1^0} h^2$ we expect this to be a minor error with respect to the aimed level of precision.

One more comment seems to be in order concerning the radiation of potentially soft photons. In the case of photons in the final state, the $2 \to 3$ real radiation process is IR divergent as the photon can become soft. As for the gluon this soft behavior would cancel if one would take the corresponding virtual corrections into account. This is, however, beyond the scope of this work as it would require the inclusion of EW corrections. To regulate the divergence we have introduced a lower bound on the photon energy similar to ΔE in Sec. III A, which did not much alter the final relic density but prevents the integration over the $2 \to 3$ phase space from becoming numerically unstable[4].

Further, we have introduced electron and muon masses, $m_e = 5.1 \cdot 10^{-4}$ GeV and $m_\mu = 0.106$ GeV, to keep the photon propagator in the last diagram of Fig. 4 away from its mass shell.

For consistency all changes including the associated lepton-Higgs couplings have been implemented in `CalcHEP` and are used by `micrOMEGAs` in our analysis. In addition, our `DM@NLO` package includes a lower bound on the squark width, by default taken from `micrOMEGAs`, to stabilize the integration in the vicinity of squark-propagator poles. Its value is fixed to 0.01 GeV.

---

[3] See also the vanishing weighting factor of the thermal distribution for $v \approx 0$ ($m_{\tilde{t}_1} v \ll T_{\text{freeze-out}}$), e.g., in Fig. 6.

[4] The $2 \to 3$ corrections turn out to be only a tiny contribution to $\Omega_{\tilde{\chi}_1^0} h^2$ for most of the relevant channels (see Sec. IV A), and channels with photon final states are in general less important (Sec. II).
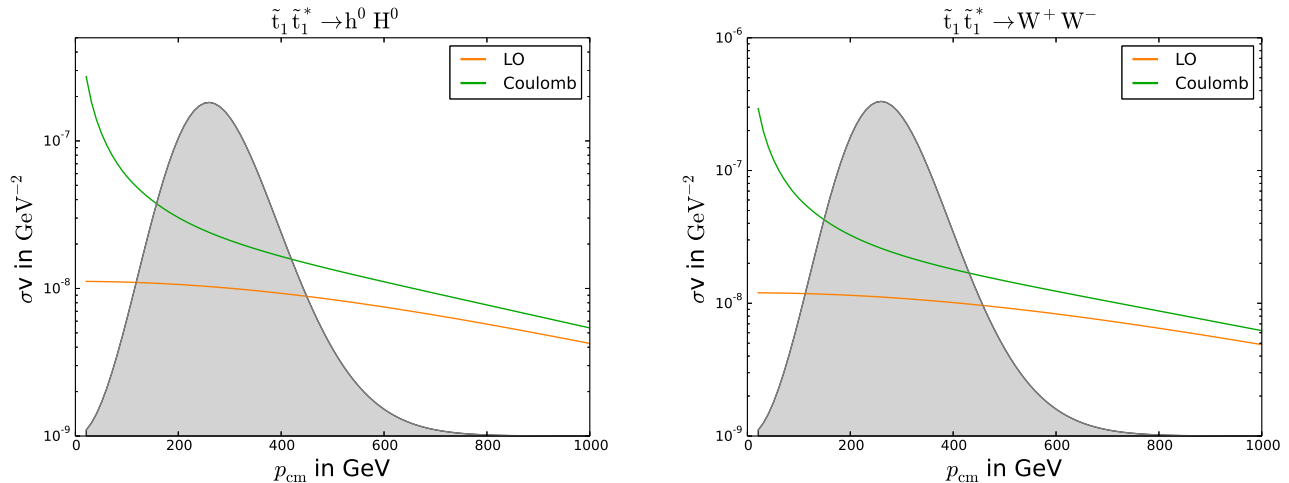
FIG. 6. The leading-order (orange line) and the Coulomb-corrected cross section (green line) multiplied with the relative velocity v in dependence of the center-of-mass momentum $p_{\rm cm}$ for two selected channels of scenario II. The grey areas indicate the thermal distribution (in arbitrary units).
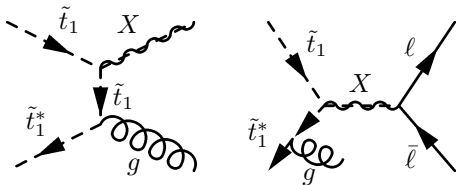

FIG. 7. Example for a potential double-counting between $2 \to 2$ and $2 \to 3$ amplitudes for a $\ell\bar{\ell}$ final state.

IV. NUMERICAL RESULTS

A. Impact on the cross section

We now turn to the discussion of the impact of our full corrections presented in Sec. III on the processes listed in Eqs. (1.9) – (1.12). In Fig. 8, we show the cross sections multiplied by the relative velocity v as a function of the center-of-mass momentum $p_{\rm cm}$ for selected annihilation channels of the three reference scenarios presented in Tab. I. More precisely, we show the cross section at tree level (black dashed line), including the full $\mathcal{O}(\alpha_s)$ corrections as discussed in Sec. III A (red solid line), with the full corrections including the Coulomb corrections of Sec. III B (blue solid line), and the corresponding value obtained by `micrOMEGAs`/`CalcHEP` (orange solid line). The lower part of each plot contains different ratios between the four cross sections (second item in the legend). As before, the grey shaded regions represent the thermal weighting of the σv contributions to $\langle\sigma_{\rm ann}v\rangle$ in Eq. (1.4).

The upper left plot of Fig. 8 shows σv for the process $\tilde{t}_1\tilde{t}_1^* \to h^0 h^0$, which is the dominant subchannel in scenario Ia. We observe that our prediction for the cross

section at tree level deviates by roughly 45% from the `micrOMEGAs` result. This deviation can be traced back to a different treatment of couplings as well as different input parameters used within `micrOMEGAs`. In particular, `micrOMEGAs` uses the $\overline{\rm DR}$-top mass $m_{\rm t}^{\overline{\rm DR}} = 161.6$ GeV whereas we take the on-shell top mass $m_{\rm t}^{\rm OS} = 172.3$ GeV. These enter the Yukawa couplings and in turn alter the important t- and u-channels (see Tab. IV), which is the main reason for the observed shift between our tree level and the `micrOMEGAs` result. Due to the Coulomb corrections discussed in Sec. III B, the higher-order corrections (red and blue curves) rise steeply for small velocities (i.e. small $p_{\rm cm}$). For larger values of $p_{\rm cm} > 400$ GeV, the Coulomb corrections become less relevant, and the full correction converges against the $\mathcal{O}(\alpha_s)$ correction with growing $p_{\rm cm}$ whereas the $2 \to 3$ processes become more and more important and already start to significantly alter the $p_{\rm cm}$ dependence of the NLO and full result. Here, the full correction lead to a change of around 35% compared to our tree-level calculation.

Comparing the ratios $\sigma_{\rm full}/\sigma_{\rm tree}$ (red line) and $\sigma_{\rm NLO}/\sigma_{\rm tree}$ (orange line) in the lower part of the plot within the most relevant region for the calculation of $\Omega_{\tilde{\chi}_1^0}h^2$ between $p_{\rm cm} = 50$ GeV and $p_{\rm cm} = 350$ GeV, we observe that the Coulomb correction significantly contributes even beyond the NLO. Its contribution at NNLO and higher amounts up to about half of the $\mathcal{O}(\alpha_s)$ contribution. Furthermore, our full result deviates from the tree level by up to 300% and from the `micrOMEGAs` result even by up to a factor 7 to 8 within the interval between $p_{\rm cm} = 50$ GeV and 350 GeV.

In the upper right corner of Fig. 8 we show the analogous plot for the process $\tilde{t}_1\tilde{t}_1^* \to Z^0 Z^0$ of scenario Ia. Here, our tree level differs again quite strongly from the `micrOMEGAs` result by about 60%. As before this deviation can be traced back to the different treatment of
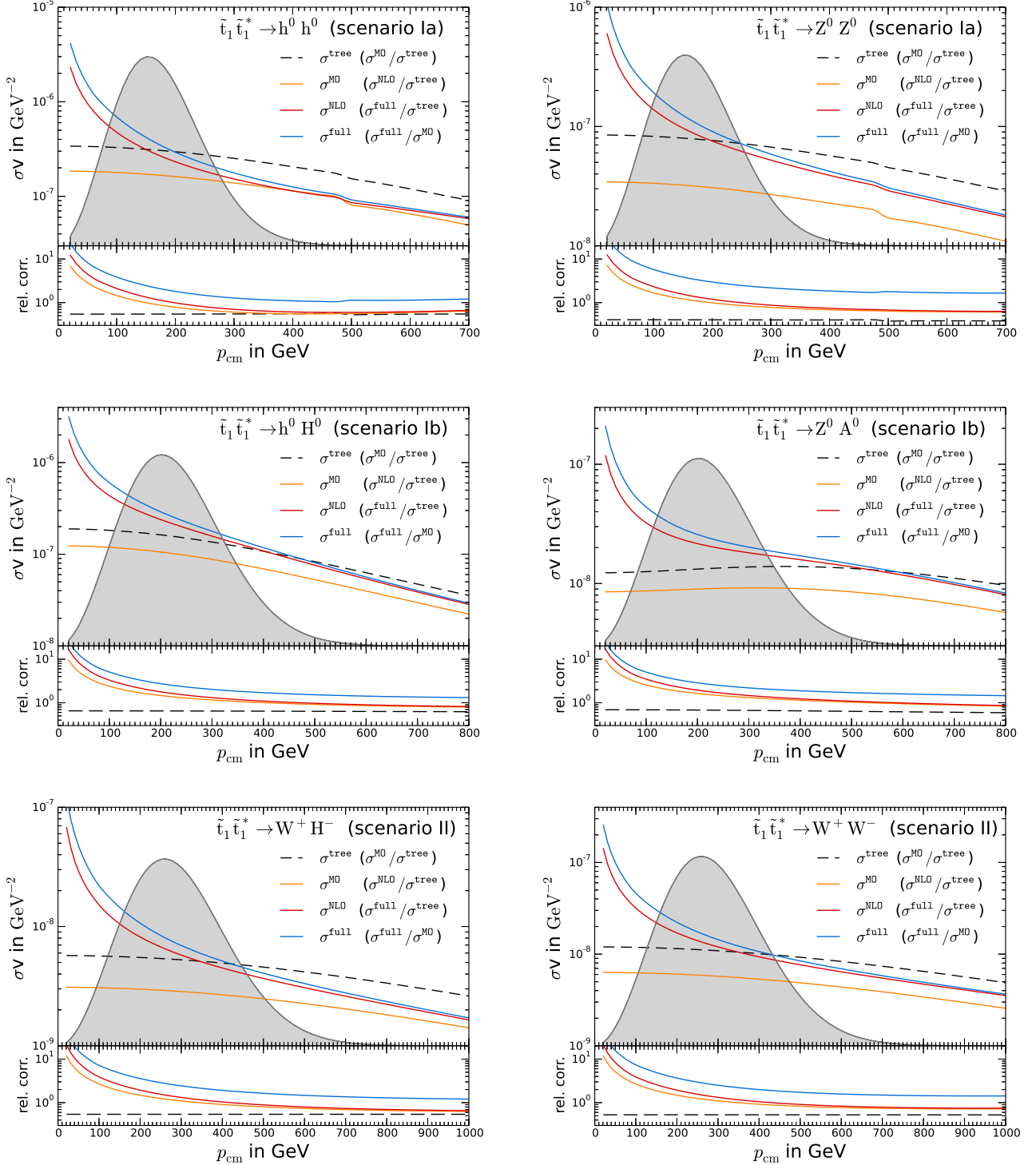
FIG. 8. Tree level (black dashed line), `micrOMEGAs` (orange solid line), NLO ($\mathcal{O}(\alpha_s)$) corrections (red solid line) and full corrections of Sec. III (blue solid line) for selected channels in the scenarios of Tab. I. The upper part of each plot shows σv in GeV^{-2} in dependence of the momentum in the center-of-mass frame p_{cm}. The grey areas indicate the thermal distribution (in arbitrary units). The lower parts of the plots show the corresponding ratios of the cross sections (second item in the legends).
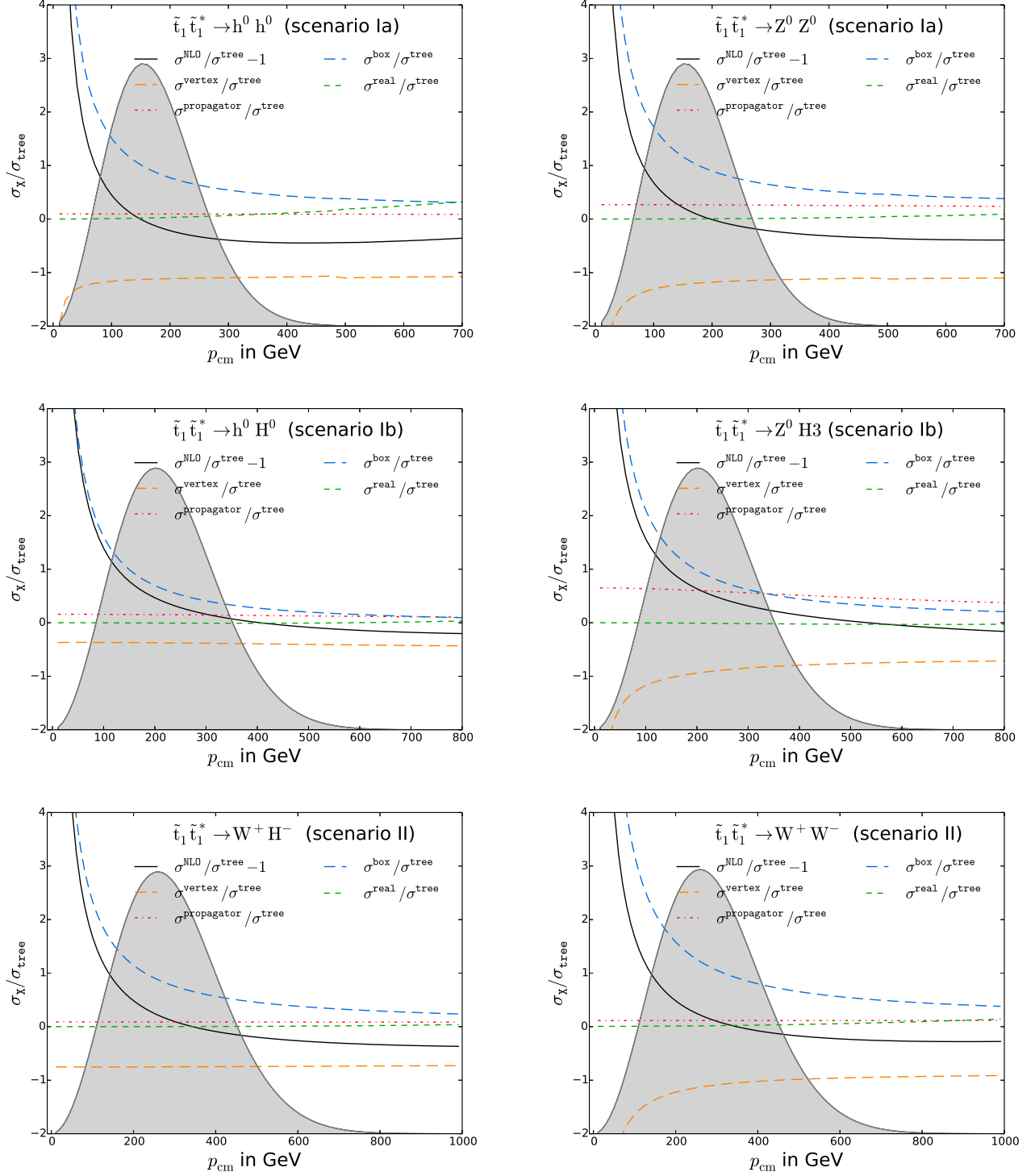
FIG. 9. Results for NLO- (without tree level, black), vertex- (orange), propagator- (red), box- (blue) and real plus soft photon corrections (green) of Sec. III A for selected channels in the scenarios of Tab. I. The plots show ratios of the different corrections over tree-level cross sections dependent on p_{cm}. The grey areas indicate the thermal distribution (in arbitrary units).

couplings and input parameters due to our choice of the renormalization scheme. For small $p_{\rm cm}$, however, the Coulomb enhancement takes again over and results in large corrections of a factor of 10 and more relative to our tree level. In the important region between $p_{\rm cm} = 50$ GeV and 350 GeV, the deviation between our full correction and our tree level amounts up to a factor 3 or 4, whereas the ratio between the full result and `micrOMEGAs` gets even larger by a factor 3 and more.

With these two final states, $h^0 h^0$ and $Z^0 Z^0$, constituting around 55% of the total annihilation cross section $\langle \sigma_{\rm ann} v \rangle$ (see Tab. III), the importance of our corrections to the neutralino relic density is already indicated at this point.

The small kinks in the upper two plots of Fig. 8 around $p_{\rm cm} = 485$ GeV are due to a very broad s-channel resonance caused by the heavier CP-even Higgs H^0. Even though the pseudoscalar Higgs boson A^0 is similar in mass ($m_{A^0} \approx m_{H^0} = 1917.4$ GeV), it does not contribute to the s-channel in the case of $\tilde{t}_1 \tilde{t}_1^*$ annihilation (see Sec. II) as it is CP-odd.

The remaining four plots show $\tilde{t}_1 \tilde{t}_1^* \rightarrow h^0 H^0$ and $\tilde{t}_1 \tilde{t}_1^* \rightarrow Z^0 A^0$ for scenario Ib and $\tilde{t}_1 \tilde{t}_1^* \rightarrow W^+ H^-$ and $\tilde{t}_1 \tilde{t}_1^* \rightarrow W^+ W^-$ for scenario II. In all four cases our tree level differs quite strongly from the `micrOMEGAs` result by up to roughly 50%. But although the $Z^0 A^0$ final state is quite similar to the $Z^0 Z^0$ final state the deviation between our tree level and `micrOMEGAs` is in the former case only half as large as in the latter case. The large difference seen in the case of the $Z^0 Z^0$ final state comes, beside the different treatment of the top mass, from the longitudinal polarized vector bosons which are in the Feynman gauge represented by the Goldstone bosons G^0. More accurately, it is the coupling $\tilde{t}_1 \tilde{t}_2 G^0$ that causes the large difference in Fig. 8. It is treated differently in `micrOMEGAs` and enters the t- and u-channel contributions twice in the case of $Z^0 Z^0$ but only once, e.g., if the final state is $Z^0 A^0$.

In the last four plots, the Coulomb corrections dominate our higher-order corrections in the region of small $p_{\rm cm}$. For large values of $p_{\rm cm}$, however, the full $\mathcal{O}(\alpha_s)$ corrections become relevant and give rise to corrections between roughly 15% and 35%. In the region relevant for $\Omega_{\tilde{\chi}_1^0} h^2$, i.e. in the vicinity of the peak of the thermal distribution, the deviation between our full result and our tree level accounts for roughly 50% to 100% and between our full result and `micrOMEGAs` for around 200 %.

In Fig. 9, we present the decomposition of the absolute value of the NLO cross section without tree level contributions $\sigma^{\rm NLO}/\sigma^{\rm tree} - 1$ (black) into the various types of UV finite $\mathcal{O}(\alpha_s)$ corrections for each of the processes of Fig. 8. More precisely, we show the vertex (orange), propagator (red), box (blue) and real corrections (green), where the latter also contain the soft gluon contribution as discussed in Sec. III A. All contributions are normalized to the tree-level cross section. Although all these contributions are UV finite, the vertex, box, and real corrections are separately IR divergent as well as dependent

on large logarithms of the regularization scale μ. These logarithms cancel between the individual contributions of Fig. 9.

Comparing the different contributions for each process, one can clearly identify the subclasses of $\mathcal{O}(\alpha_s)$ corrections, which are enhanced by the Coulomb corrections of Sec. III B, namely the vertex and box corrections. Only the vertex corrections of the processes $\tilde{t}_1 \tilde{t}_1^* \rightarrow h^0 H^0$ and $\tilde{t}_1 \tilde{t}_1^* \rightarrow W^+ H^-$ show no significant rise at small $p_{\rm cm}$. This is due to the dominant t- and $u-$ channels contributions for these cases, which turn out to be much larger than the Coulomb enhanced diagrams subsumed under the vertex corrections (see Tab. IV). Hence one has to go to much smaller $p_{\rm cm} \sim \mathcal{O}(10^{-3}\,{\rm GeV})$ to see a significant rise in the vertex corrections, which is, however, not shown here.

The sum of box- and vertex corrections result in a positive correction at low $p_{\rm cm}$. For large $p_{\rm cm}$, however, the situation is reversed and the overall corrections are negative. The point where the overall correction changes its sign is clearly visible in each plot and is given by the point where the box and vertex contributions are roughly the same. The real emission corrections are subdominant in all cases and rise only for larger $p_{\rm cm}$, where the larger kinematically accessible phase space of the $2 \rightarrow 3$ processes enhances the associated total cross sections.

B. Impact on the relic density

In this subsection, we investigate the impact of our corrections on the neutralino relic density $\Omega_{\tilde{\chi}_1^0} h^2$. For the following analysis, we have implemented our results into a computer code called `DM@NLO` that can be linked to `micrOMEGAs`. In total we correct 24 different final states of $\tilde{t}_1 \tilde{t}_1^*$ pair annihilation. Although most of them contribute only marginally to the final relic density, the relevance of each of the different processes is a priori unknown as it depends strongly on the specific scenario. This makes a comprehensive study of each point of the parameter space necessary.

As the NLO corrections are more time consuming than the regular tree-level calculation, we optimize our numerical evaluation by calculating the NLO corrections only for processes which contribute more than 1% to the total annihilation cross section. This is in accordance with the current experimental precision of $\Omega_{\tilde{\chi}_1^0} h^2$, which is around 2% at 1σ confidence level. The remaining channels are either replaced for consistency by our tree level or are left unchanged.

We present our results in the M_1-$M_{\tilde{u}_3}$ plane of the pMSSM parameter space defined in Sec. II. These two parameters influence directly the masses of the lightest neutralino and the lightest scalar top quark, respectively, and thus the mass splitting $m_{\tilde{\chi}_1^0} - m_{\tilde{t}_1}$ to which $\tilde{t}_1 \tilde{t}_1^*$ pair annihilation is extremely sensitive with respect to the relic density. In our scenarios the lightest neutralino is always bino-like and hence is its mass predominantly de-
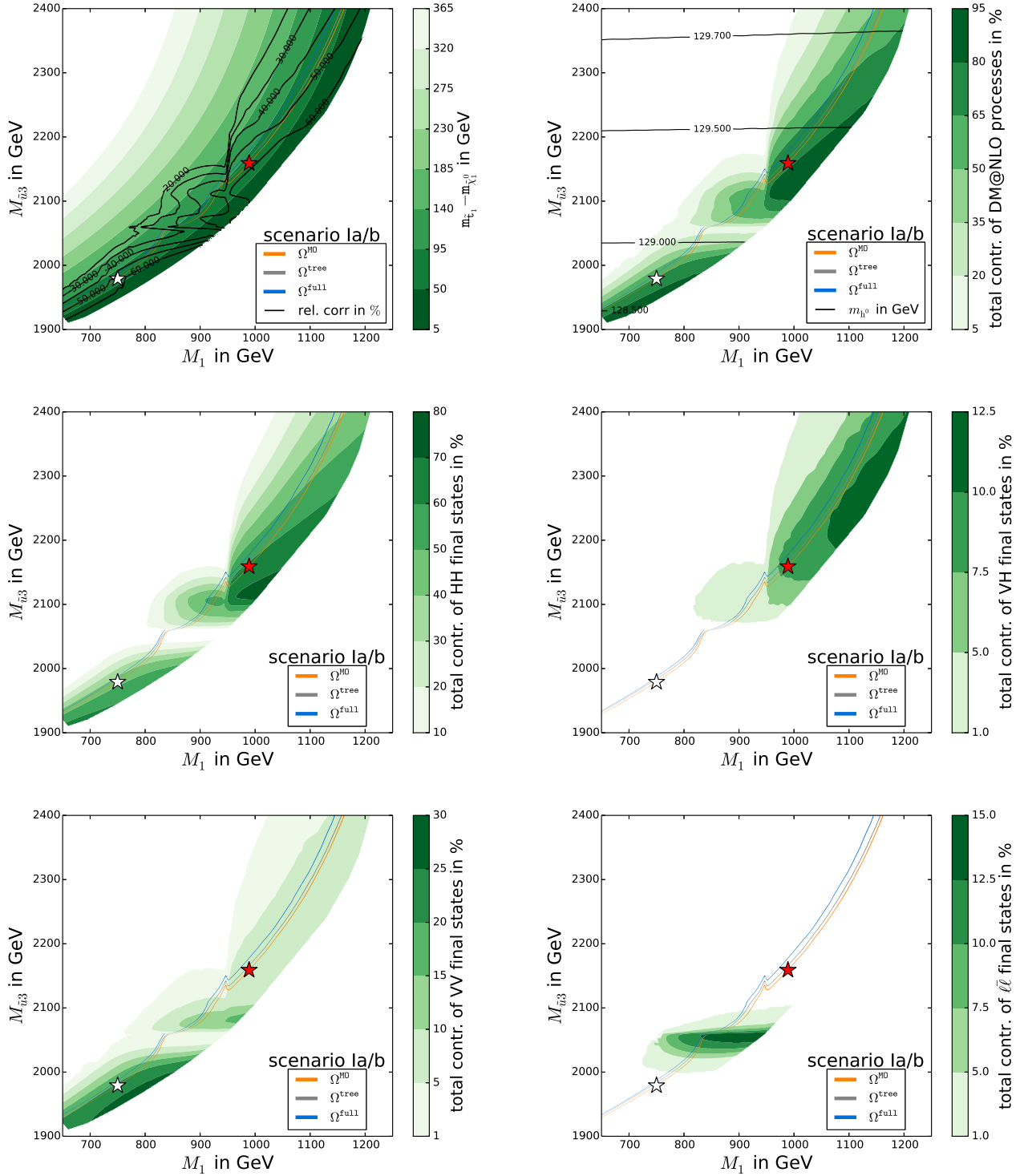
FIG. 10. Planck-compatible relic density bands (see Eq. 1.1) in the M_1–$M_{\tilde{u}_3}$ plane surrounding scenario Ia and Ib. The calculation includes `micrOMEGAs` (orange), our tree-level (grey) and our full corrections (blue). The white and red stars mark the positions of our reference scenarios Ia and Ib. The black lines in the upper left plot show the deviation between `micrOMEGAs` and our full result in per cent. In the upper right plot the black lines stand for the mass of the lightest Higgs boson m_{h^0} in GeV. For further explanations see the text.
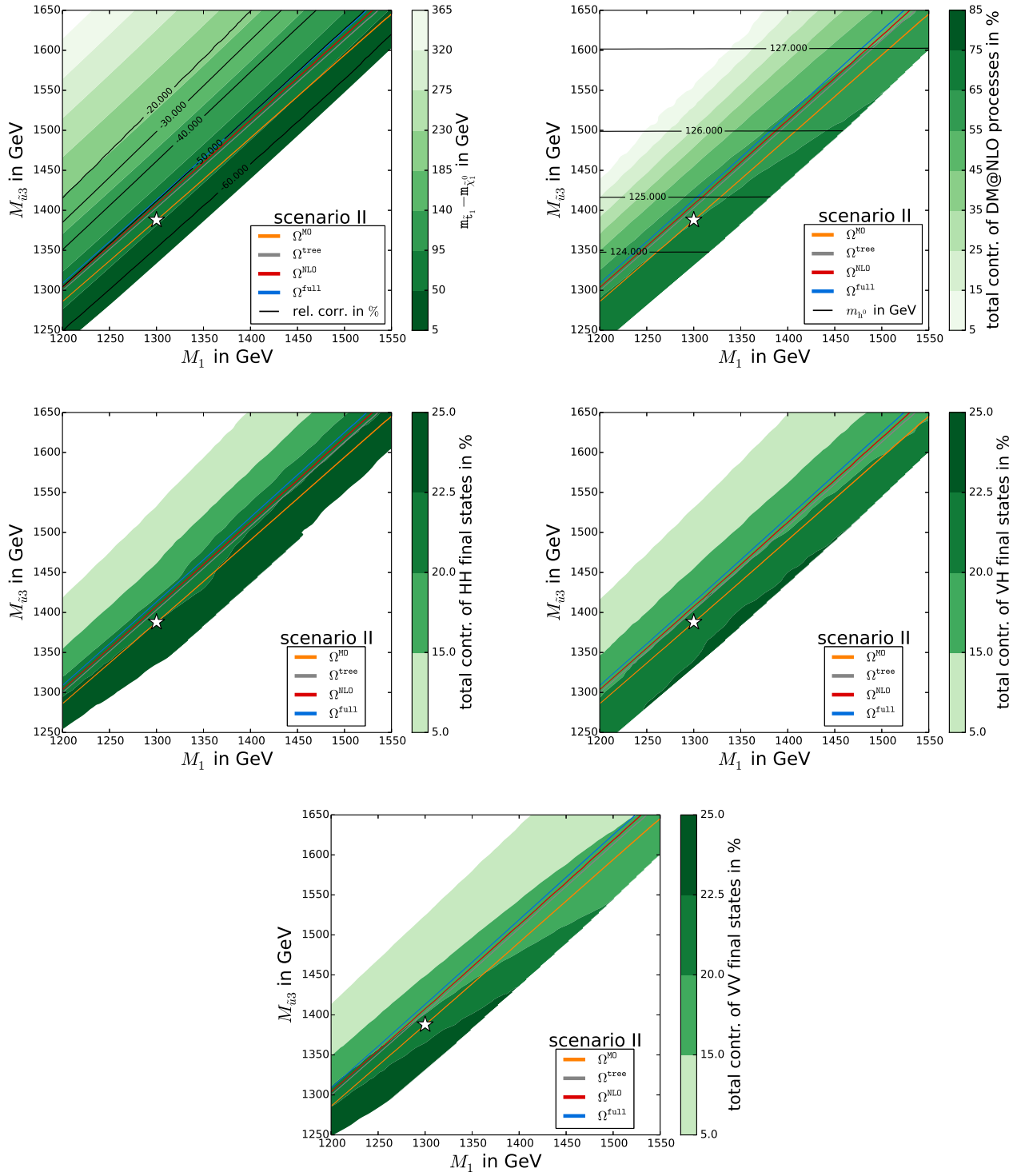
FIG. 11. Same as Fig. 10 for scenario II, but here the plot for the $\ell\bar{\ell}$-final states is left out (see text). We further added the NLO result in red.

termined by the M_1 parameter. The lightest scalar top quark possesses a large admixture of $\tilde{t}_R$, the superpartner of the right-handed part of the top quark, and so the mass is also sensitive to the right-handed supersymmetry breaking parameter $M_{\tilde{u}_3}$ (see Tab. II).

In Figs. 10 and 11, we present scans around our reference scenarios of Tab. I. The orange band ($\Omega^{\tt MO}$) refers to the relic density $\Omega_{\tilde{\chi}_1^0}h^2$ obtained by `micrOMEGAs`/`CalcHEP`, the grey band ($\Omega^{\tt tree}$) indicates the prediction of the relic density $\Omega_{\tilde{\chi}_1^0}h^2$ where our tree level calculation replaces the `CalcHEP` result for the processes specified in Eqs. (1.9) – (1.12), and the blue band ($\Omega^{\tt full}$) shows the neutralino relic density $\Omega_{\tilde{\chi}_1^0}h^2$ as a result of our full calculation discussed in Sec. III. We further added to Fig. (11) in red the relic density obtained by our NLO calculation.

The experimental 1σ-uncertainty is reflected by the width of the three bands in Figs. 10 and 11. The narrow band demonstrates how constraining the assumption that the lightest neutralino $\tilde{\chi}_1^0$ accounts for the whole cold dark matter in the universe actually is. We encounter a distinct separation between the bands corresponding to our tree level result (grey) and the default result of `micrOMEGAs` (orange) in all plots nearly everywhere over the whole $M_1 - M_{\tilde{u}_3}$ plane. This separation gets even enhanced if one takes the NLO (red) or full (blue) corrections into account. The black contour lines in the top left plots of Figs. 10 and 11 quantify more precisely the magnitude of the corrections between `micrOMEGAs` and our full result. They amount up to roughly 50% in Fig. 11 and reach even more than 50% in the cosmologically favored region of the corresponding plot of Fig. 10. Within the same regions, our fully corrected result deviates from our tree level by up to 25% in Fig. 11 and by nearly 40% in Fig. 10 respectively. One can further see in Fig. 11 the importance of the NNLO Coulomb corrections for a precise estimation of the relic density. The full result deviates by far more than one standard deviation from our NLO result, which is visible in the splitting of the associated blue and red bands. The deviation due to Coulomb corrections of NNLO and beyond even exceeds the size of our full NLO corrections. Beside the fact, that for $v \approx \alpha_s$ the higher order Coulomb corrections are roughly of the same size as the leading order Coulomb corrections, this result can be further traced back to a cancellation among the NLO contributions to the relic density. Fig. 8 shows, that the NLO corrections at large v tend to lower the tree level cross section, whereas at lower v the Coulomb corrections start to alter the cross section turning the NLO corrections to positive values. Since this transition happens to be for certain processes relatively close to the peak of the thermal distribution, the associated cancellation significantly lowers the total contribution of the NLO corrections to the relic density and in turn raises the importance of the throughout positive higher order

Coulomb corrections[5].

Apart from the corrections discussed above, Figs. 10 and 11 highlight several regions of parameter space where different processes dominate the total annihilation cross section. The cosmologically preferred region of parameter space lies along a line of almost constant mass difference between the LSP and the NLSP. In both scenarios, the regions where the processes investigated in this analysis are important stretch along the favored region of parameter space. For scenario Ia/b, one observes that for higher values of $M_{\tilde{u}_3}$ (that means for heavier scalar top quarks) along the favored region the processes with Higgs bosons in the final state dominate. On the other end of the favored region where $M_{\tilde{u}_3}$ and M_1 are smaller, the processes with a vector boson in the final state takes over to be most important. Here the stops are lighter and two Higgs bosons in the final state are no longer kinematically allowed or are at least largely suppressed. The same observation but less pronounced holds for scenario II, where in the last plot of Fig. 11 one encounters an increasing relevance of vector-vector final states towards lower values of $M_{\tilde{u}_3}$ and M_1.

Although both scenarios fulfill the experimental bounds on the Higgs boson mass, only scenario II falls into the vicinity of the experimentally favored mass m_{h^0} while the scenarios Ia and Ib already lie at the edge of the experimental constraint as given in Eq. (2.3). The mass of the lightest Higgs boson is mainly driven by the $M_{\tilde{u}_3}$ parameter as it determines the mass $m_{\tilde{t}_1}$ in our scenarios. The parameter $M_{\tilde{u}_3}$ therefore influences the mass splitting between the top quark and its superpartner $\tilde{t}_1$, which in turn enters the mass corrections of the mass of the lightest Higgs boson (see Eq. (2.1)).

Another interesting contribution with electroweak final states, which we have not mentioned yet, is the annihilation of scalar top quarks into lepton-anti-lepton pairs. Although this process is not the leading contribution to the total cross section in any of our scenarios, there is a region in the $M_{\tilde{u}_3}$-M_1 plane shown in the bottom-right plot of Fig. 10, where the process with $\tau\bar{\tau}$ final state contributes as much as 13%. In Fig. 12, we show a zoom into this area of enhanced $\tau\bar{\tau}$ contributions. It can be observed that the enhancement of the $\tau\bar{\tau}$ final state is due to an s-channel resonance caused by the heavier Higgs H^0 together with the Yukawa coupling, which for $\tan\beta = 16.3$ favors the down-type fermions. Interestingly, the corrections to this process are significant enough to cause a shift of the relic density of more than 20% relative to our tree level and even of more than 30% relative to `micrOMEGAs` despite the fact that its contribution is comparatively low. The reason is that the annihilation into $\tau\bar{\tau}$ proceeds only through an s-channel exchange of vector and Higgs bosons. As can be seen in Fig. 9, for all

---

[5] Note, that this also increases the dependence of the final relic density on the choice of μ_G. We postpone a more detailed analysis to later investigations.
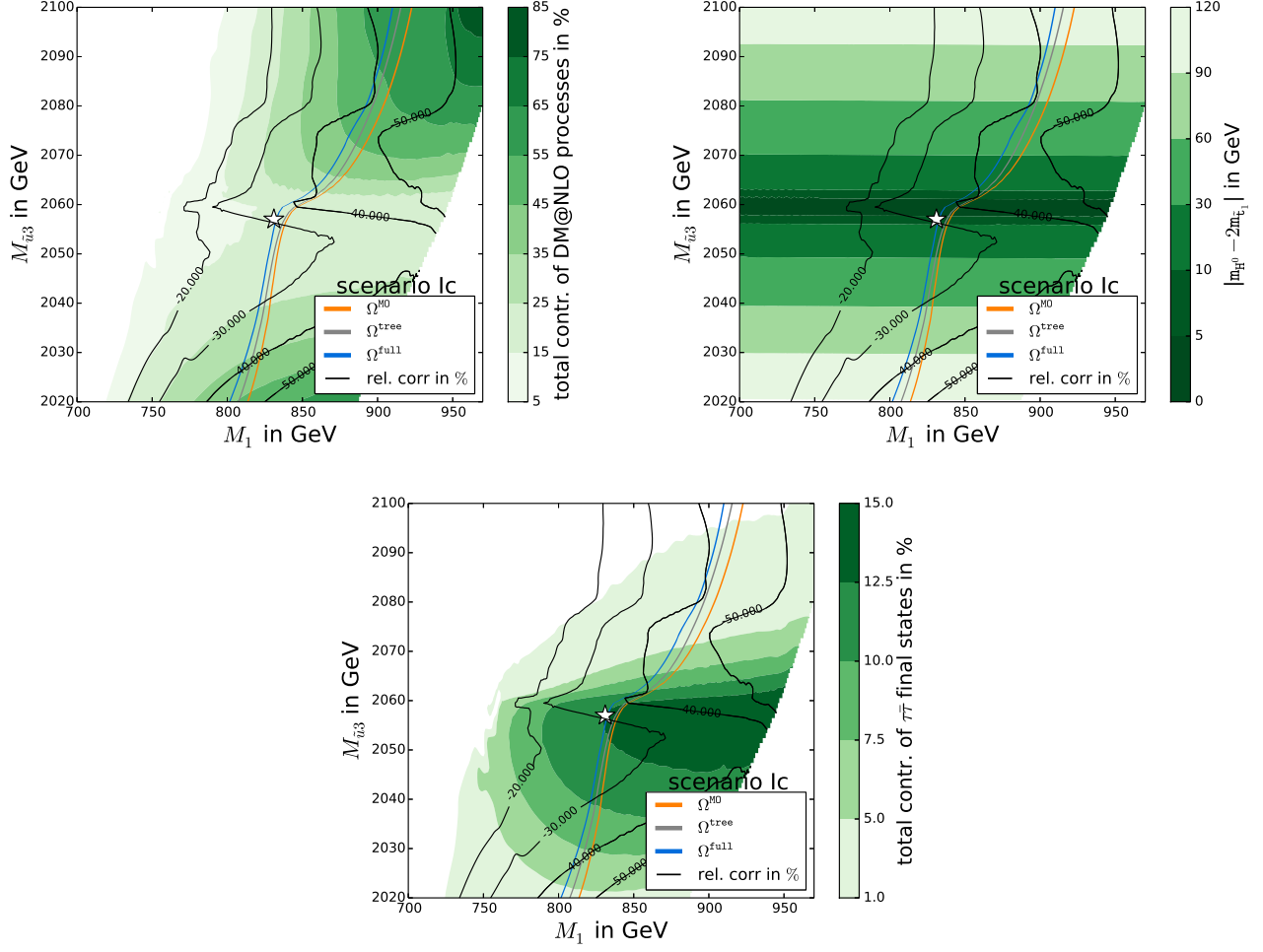
FIG. 12. Scan over the scenario Ia/b-plane. The white star marks the position of the scenario Ic ($M_1 = 831$ GeV, $M_{\tilde{u}_3} = 2057$ GeV) further analyzed in Fig. 13.
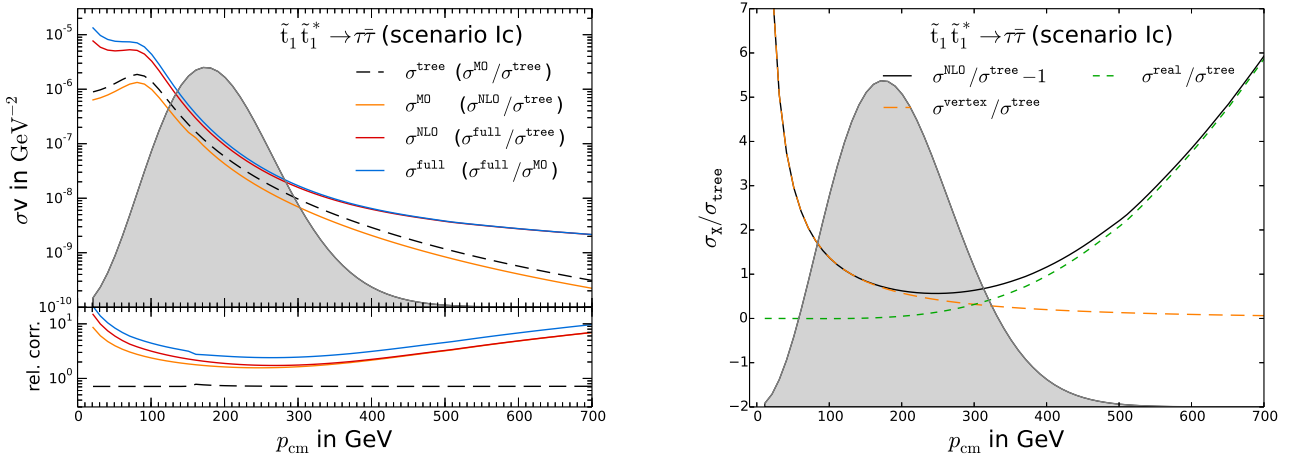

FIG. 13. Cross sections and NLO contributions to scenario Ic of Fig. 12

other final states the corrections from the vertex and the box diagrams cancel each other and lead to a reduction in the total correction. This is, however, not the case for τ-leptons in the final state as no box diagrams exist and thus, this cancellation cannot take place. For further discussion, we introduced a representative scenario Ic marked by the white star in Fig. 12. The relevant cross section contributions for this parameter point are shown in more detail in Fig. 13. We see that the corrections to the annihilation into $\tau\bar{\tau}$ are dominated by the vertex corrections and the real correction with the corresponding large Coulomb enhancement of the vertex corrections for small p_{cm}. One observes that starting at the H^0-resonance at around $p_{\mathrm{cm}} = 80$ GeV (first plot of Fig. 13) the corrections are comprised of large Coulomb corrections stemming from the vertex diagrams. Later for larger p_{cm} the corrections are dominated by the relatively large contributions of the $2 \rightarrow 3$ processes (see second plot of Fig. 13) due to the phase-space enhancement of the $2 \rightarrow 3$ final states, which sets in already for much lower p_{cm} because of the small τ-mass. Finally note that the s-wave contribution to the stop-annihilation cross section into $\ell\bar{\ell}$ final states is suppressed by a factor $(m_\ell/m_{\tilde{t}_1})^2$. Therefore a more elaborate treatment, which takes the full Coulomb corrections for the p-wave into account, may lead to relative corrections on the particular cross section, which are less suppressed than $\mathcal{O}(\alpha_s^2)$ compared to the leading order (see Sec. III B). However, as the leptons unfold their main impact on the relic density in the vicinity of the H^0-resonance, this in turn decreases the impact of the p-wave contributions (see left plot in Fig. (13)). Hence we leave this for further investigations.

V. CONCLUSIONS

An important mechanism for enhancing the annihilation cross section of the lightest neutralino in order to meet the experimentally determined value for the relic density $\Omega_{\tilde{\chi}_1^0 h^2}$ are (co)annihilation processes of nearly mass degenerate particles. A theoretically well motivated candidate for such (co)annihilation processes is the lightest stop $\tilde{t}_1$. Motivated by previous analyses [10, 11, 13], we investigated the impact of $\tilde{t}_1\tilde{t}_1^*$ annihilation into electroweak final states on the neutralino relic density including the full $\mathcal{O}(\alpha_s)$ corrections as well as the Coulomb corrections due to the exchange of soft gluons between the incoming stop-anti-stop pair.

We further explored their impact on the neutralino relic density $\Omega_{\tilde{\chi}_1^0} h^2$ within the phenomenological MSSM. For this purpose, we chose three reference scenarios, which are allowed by current experimental constraints and possess a rich variety of stop annihilation channels contributing to the relic density $\Omega_{\tilde{\chi}_1^0} h^2$. We performed large scans around these scenarios and compared the resulting $\Omega_{\tilde{\chi}_1^0} h^2$ by using the public code `micrOMEGAs`

with our results. We found that within these scenarios our results can change the neutralino relic density $\Omega_{\tilde{\chi}_1^0} h^2$ within the cosmologically favored region by more than 50%, shifting the relic band by a few tens of GeV within some of the considered pMSSM parameters. They are therefore larger than the current experimental uncertainty coming from the latest Planck data. In these cases, both the full $\mathcal{O}(\alpha_s)$ corrections as well as the Coulomb corrections of $\mathcal{O}(\alpha_s^2)$ and beyond turned out to have a sizable impact on the cross sections within the kinematically relevant region. Further, we have split the annihilation cross section into contributions stemming separately from different types of final states and analyzed vector-vector, vector-Higgs, Higgs-Higgs and lepton-anti-lepton final states. Although the Higgs-Higgs final states turned out to be enhanced by large couplings due to a large A_t favored by scenarios containing a light stop, we also found regions within the parameter space where vector-vector and vector-Higgs final states contribute sizably to $\Omega_{\tilde{\chi}_1^0} h^2$. The lepton-anti-lepton final states do not contribute as much as the other final states, but nevertheless their corrections are sizable and can lead to a significant change in $\Omega_{\tilde{\chi}_1^0} h^2$ due to the absence of large cancellations between box and vertex corrections.

We conclude, that the identification of cosmologically favored regions at the currently available level of precision requires to take into account the next-to-leading order as well as the Coulomb corrections including those investigated in this work.

Appendix A: Hypergeometric function

The hypergeometric function is defined as

$$_pF_q(a_1, a_2, ..., a_p; b_1, b_2, ..., b_q; z) = \tag{A1}$$
$$\sum_{n=0}^{\infty} \frac{(a_1)_n (a_2)_n \ldots (a_p)_n}{(b_1)_n (b_2)_n \ldots (b_q)_n} \frac{z^n}{n!}$$

with the restriction $b_i \neq 0, -1, ...$ for $i = 1, 2, ..., q$, where $(x)_n = \Gamma(x + n)/\Gamma(x)$ are the Pochhammer symbols.

The series defined by Eq. (A1) converges for $_4\mathrm{F}_3(1,1,1,1;2,2,1-\kappa;1)$, if

$$\Re\left\{\sum_{n=1}^{q}b_n - \sum_{n=1}^{q+1}a_n\right\} > 0. \tag{A2}$$

To improve on the convergence of this series we have repeatedly employed

$$\begin{aligned}
_4\mathrm{F}_3(1,1,1,1;a,a,x;1) =& \frac{1}{a^2 x(x-2(2-a))(a-x)^2}\bigg[a^2(x-1)^4 \,_4\mathrm{F}_3(1,1,1,1;a,a,x+1;1) \\
& + a(a-1)^3 x(3a+1-4x) \,_4\mathrm{F}_3(1,1,1,1;a+1,a,x;1) \\
& + (a-1)^4 x(x-a) \,_4\mathrm{F}_3(1,1,1,1;a+1,a+1,x;1)\bigg],
\end{aligned} \tag{A3}$$

$$\begin{aligned}
_4\mathrm{F}_3(1,1,1,1;a,b,x;1) =& \frac{1}{a+b+x-4}\bigg[\frac{(a-1)^4}{a(a-b)(a-x)} \,_4\mathrm{F}_3(1,1,1,1;a+1,b,x;1) \\
& + \frac{(b-1)^4}{b(b-a)(b-x)} \,_4\mathrm{F}_3(1,1,1,1;a,b+1,x;1) + \frac{(x-1)^4}{x(x-a)(x-b)}\,_4\mathrm{F}_3(1,1,1,1;a,b,x+1;1)\bigg],
\end{aligned} \tag{A4}$$

which is valid for $x \neq -1, -2, \dots$ and $a, b \in \mathbb{N}/\{0,1\}$, $a \neq b$ [42, 50].

[1] P. A. R. Ade *et al.* [Planck Collaboration], Astron. Astrophys. (2014) [arXiv:1303.5076v3 [astro-ph.CO]].

[2] The WMAP collaboration, E. Komatsu *et al.*, Astrophys. J. Suppl. **208** (2013) 20 arXiv:1212.5225 [astro-ph.CO]

[3] P. Gondolo and G. Gelmini, Nucl. Phys. B **360** (1991) 145.

[4] J. Edsjö and P. Gondolo, Phys. Rev. D **56** (1997) 1879 [arXiv:hep-ph/9704361].

[5] P. Binetruy, G. Girardi and P. Salati, Nucl. Phys. B **237** 285 (1984).

[6] K. Griest and D. Seckel, Phys. Rev. D **43** (1991) 3191.

[7] T. Han, Z. Liu and A. Natarajan, JHEP **1311** 008 (2013) [arXiv:1303.3040v2 [hep-ph]].

[8] J. Ellis, K. A. Olive and Y. Santoso, [arXiv:0112113v1 [hep-ph]].

[9] B. Herrmann and M. Klasen, Phys. Rev. D **76** (2007) 117704 [arXiv:0709.0043 [hep-ph]].
B. Herrmann, M. Klasen and K. Kovarik, Phys. Rev. D **80** (2009) 085025 [arXiv:0907.0030 [hep-ph]].

[10] B. Herrmann, M. Klasen and K. Kovarik, Phys. Rev. D **79** (2009) 061701 [arXiv:0901.0481 [hep-ph]].

[11] B. Herrmann, M. Klasen, K. Kovarik, M. Meinecke and P. Steppeler, Phys. Rev. D **89** 114012 (2014) [arXiv:1404.2931 [hep-ph]].

[12] A. Freitas, Phys. Lett. B **652** (2007) 280 [arXiv:0705.4027 [hep-ph]].

[13] J. Harz, B. Herrmann, M. Klasen, K. Kovarik and Q. Le Boulc'h, Phys. Rev. D **87** (2013) 054031 [arXiv:1212.5241 [hep-ph]].

[14] J. Harz, B. Herrmann, M. Klasen and K. Kovarik, arXiv:1409.2898 [hep-ph].

[15] N. Baro, F. Boudjema and A. Semenov, Phys. Lett. B **660** (2008) 550 [arXiv:0710.1821 [hep-ph]].
N. Baro, G. Chalons and S. Hao, AIP Conf. Proc. **1200** (2010) 1067 [arXiv:0909.3263 [hep-ph]].

N. Baro, F. Boudjema, G. Chalons and S. Hao, Phys. Rev. D **81** (2010) 015005 [arXiv:0910.3293 [hep-ph]].

[16] F. Boudjema, G. Drieu La Rochelle and S. Kulkarni, Phys. Rev. D **84** (2011) 116001 [arXiv:1108.4291 [hep-ph]].

[17] A. Chatterjee, M. Drees and S. Kulkarni, [arXiv:1209.2328 [hep-ph]].

[18] M. Beneke, F. Dighera and A. Hryczuk [arXiv:1409.3049 [astro-ph]].

[19] J. Ellis, K. A. Olive and J. Zheng, [arXiv:1404.5571v1 [hep-ph]].

[20] G. Bélanger, F. Boudjema, A. Pukhov and A. Semenov, Comput. Phys. Commun. **177** (2007) 894. G. Bélanger, F. Boudjema, A. Pukhov and A. Semenov, Comput. Phys. Commun. **149** (2002) 103 [arXiv:hep-ph/0112278].

[21] P. Gondolo, J. Edsjö, P. Ullio, L. Bergström, M. Schelke and E. A. Baltz, JCAP **0407** (2004) 008 [arXiv:astro-ph/0406204]. P. Gondolo, J. Edsjö, P. Ullio, L. Bergström, M. Schelke, E.A. Baltz, T. Bringmann and G. Duda, http://www.darksusy.org.

[22] C. Kilic and B. Tweedie [arXiv:1211.6106v2 [hep-ph]].

[23] Z.-H. Yu, X.-J. Bi, Q.-S. Yan and P.-F. Yin [arXiv:1211.2997v1 [hep-ph]].

[24] G. Aad *et al.* [ATLAS Collaboration], Phys. Lett. B **716** (2012) 1 [arXiv:1207.7214 [hep-ex]].

[25] S. Chatrchyan *et al.* [CMS Collaboration], Phys. Lett. B **716** (2012) 30 [arXiv:1207.7235 [hep-ex]].

[26] G. Aad *et al.* [ATLAS Collaboration], ATLAS-CONF-2012-170, Dec. 2012.

[27] H. E. Haber, R. Hempfling and A. H. Hoang Z. Phys. C**75** (1997) 539 [arXiv:9609331 [hep-ph]].

[28] M. Badziak, E. Dudas, M. Olechowski and S. Pokorski JHEP **1207** 155 (2012) [arXiv:1205.1675 [hep-ph]].

[29] J. A. Aguilar-Saavedra, A. Ali, B. C. Allanach, R. L. Arnowitt, H. A. Baer, J. A. Bagger, C. Balazs

and V. D. Barger *et al.*, Eur. Phys. J. C **46** (2006) 43 [arXiv:hep-ph/0511344].

[30] O. Buchmueller, M. J. Dolan, J. Ellis, T. Hahn, S. Heinemeyer, W. Hollik, J. Marrouche and K. A. Olive *et al.*, arXiv:1312.5233 [hep-ph].

[31] Y. Amhis *et al.* [Heavy Flavor Averaging Group Collaboration], arXiv:1207.1158 [hep-ex] and online update at `http://www.slac.stanford.edu/xorg/hfag`.

[32] K.A. Olive *et al.* (Particle Data Group) Chin. Phys. C **38** (2014) 090001

[33] W. Porod, Comput. Phys. Commun. **153** (2003) 275 [arXiv:hep-ph/0301101]
W. Porod and F. Staub, Comput. Phys. Commun. **183** (2012) 2458 [arXiv:1104.1573 [hep-ph]].

[34] A. Belyaev, N. D. Christensen and A. Pukhov, Comput. Phys. Commun. **184** (2013) 1729 [arXiv:1207.6082v2 [hep-ph]].

[35] G. 't Hooft and M. Veltman Nucl. Phys. B **153** (1979) 365

[36] F. Bloch and A. Nordsieck, Phys. Rev. **52** 54 (1937). T. Kinoshita, J. Math. Phys. **3** (1962) 650. T. D. Lee and M. Nauenberg, Phys. Rev. **133** (1964) B1549.

[37] S. Catani, S. Dittmaier, M. H. Seymour and Z. Trocsanyi, Nucl. Phys. B **627** (2002) 189 [hep-ph/0201036].

[38] M. Beneke, A. Signer and V. A. Smirnov, Phys. Lett. B **454** (1999) 137 [arXiv:9903260v1 [hep-ph]].

[39] A. Pineda and A. Signer, Nucl. Phys. B **762** (2007) 67 [arXiv:0607239v1[hep-ph]].

[40] G. T. Bodwin, E. Braaten and G. P. Lepage, Phys. Rev. D **51** (1995) 1125 [arXiv:9407339v2[hep-ph]].

[41] M. J. Strassler and M. E. Peskin, Phys. Rev. D **43** (1991) 1500

[42] M. R. Kauth, J. H. Kühn, P. Marquard and M. Steinhauser, Nucl. Phys. B **857** (2012) 28 [arXiv:1108.0361v2 [hep-ph]].

[43] Y. Kiyo, J. H. Kühn, S. Moch, M. Steinhauser and P. Uwer, Eur. Phys. J. C **60** (2009) 375 [arXiv:0812.0919v2 [hep-ph]].

[44] M. Beneke, [arXiv:9911490v1[hep-ph]].

[45] M. Beneke, P. Falgari and C. Schwinn Nucl. Phys. **B842** (2011) 414 [arXiv:1007.5414v2[hep-ph]].

[46] M. Beneke, Y. Kiyo and K. Schuller, Nucl. Phys. B **714** (2005) 67. [arXiv:0501289v2 [hep-ph]].

[47] M. R. Kauth, J. H. Kühn, P. Marquard and M. Steinhauser, Nucl. Phys. B **831** (2010) 285 [arXiv:0910.2612v1 [hep-ph]].

[48] R. Iengo, JHEP **0905** (2009) 024 [arXiv:0902.0688v3 [hep-ph]].

[49] S. Cassel, J. Phys. G **37** (2010) 105009 [arXiv:0903.5307v1 [hep-ph]].

[50] T. Huber and D. Maître, Comput. Phys. Commun. **175** (2006) 122 [arXiv:0507094v2 [hep-ph]].